Rapid prediction of electric fields associated with geomagnetically induced currents in the presence of three-dimensional ground structure: Projection of remote magnetic observatory data through magnetotelluric impedance tensors

L R. Bonner[1], and Adam Schultz[1]

[1]College of Earth, Ocean and Atmospheric Sciences, Oregon State University, Corvallis OR 97331-5503, USA.

Corresponding author: Adam Schultz (Adam.Schultz@oregonstate.edu)

Key Points:

- Ground electric fields due to GICs are non-uniform for an Earth with 3-D electrical conductivity structure.
- It is computationally burdensome to solve for electric and magnetic fields in the coupled 3-D ionosphere-Earth system.
- Electric fields are estimated rapidly by projecting magnetic observatory data through MT impedance tensors.

This article has been accepted for publication and undergone full peer review but has not been through the copyediting, typesetting, pagination and proofreading process which may lead to differences between this version and the Version of Record. Please cite this article as doi: 10.1002/2016SW001535

Abstract

Ground level electric fields arising from geomagnetic disturbances (GMDs) are used by the electric power industry to calculate geomagnetically induced currents (GICs) in the power grid. Current industry practice is limited to electric fields associated with 1-D ground electrical conductivity structure, yet at any given depth in the crust and mantle lateral (3-D) variations in conductivity can span at least three orders of magnitude, resulting in large deviations in electric fields relative to 1-D models. Solving Maxwell's equations for electric fields associated with GMDs above a 3-D Earth is computationally burdensome and currently impractical for industrial applications. A computationally light algorithm is proposed as an alternative. Real-time data from magnetic observatories are projected through multivariate transfer functions to locations of previously occupied magnetotelluric (MT) stations. MT time series and impedance tensors, such as those publically available from the NSF EarthScope Program, are used to scale the projected magnetic observatory data into local electric field predictions that can then be interpolated onto points along power grid transmission lines to actively improve resilience through GIC modeling. Preliminary electric field predictions are tested against previously recorded time series, idealized transfer function cases, and existing industry methods to assess the validity of the algorithm for potential adoption by the power industry. Some limitations such as long period diurnal drift are addressed, and solutions are suggested to further improve the method before direct comparisons with actual GIC measurements are made.

1 Introduction

GICs are quasi-DC signals that result from GMDs that perturb the Earth's electric and magnetic field through inductive coupling between ionospheric (source) currents and currents induced in response in the oceans, crust and mantle. GICs are capable of causing significant structural damage to pipelines and other built infrastructure through corrosion, and they can severely impact electric power transmission grids through premature ageing and failure of transformers [Pirjola, Viljanen et al., 2000]. In the case of electric power systems, strong currents are able to enter the grounding of transformers and saturate the cores, which can distort the AC waveform of the power signal, leading to a host of other problems such as system relay interference, reactive power loss, or even total system collapse [Molinski, 2002]. There are several examples of geomagnetic storms that have caused GIC related damage to power grids and to cabled communications systems; the two most widely known being the Carrington event in 1859, where induced currents caused widespread damage to telegraph infrastructure across Europe and North America, and the Hydro-Quebec blackout of 1989, which left Quebec without power for 9 hours and almost cascaded across the eastern seaboard of the United States [Boteler et al., 1998], resulting in half-cycle saturation of and serious damage to a nuclear unit transformer in Salem, New Jersey. A variety of factors control the strength of GMDs, such as the 11-year sunspot cycle, episodic coronal mass ejection patterns, and seasonal magnetic field coupling that are capable of combining constructively, so the threat to power resilience is both continual and grave. In particular, a 100-year GIC scenario is estimated to potentially produce ground level electric fields at high geomagnetic latitudes ranging from 5 to 20 V/km, depending on ground (crust and mantle) electrical conductivity structure [Pulkkinen et al., 2012; Love et al., 2016], which could cause serious damage to increasingly integrated and vital electrical systems.

GICs are particularly strong at high latitudes where extreme electromagnetic field events associated with auroral excitations and electrojet currents are more prevalent [Ngwira et al., 2013] and where continental shield areas (e.g. Canadian Shield and Fennoscandia) contain blocks of electrically resistive crustal sections [Cherevatova, et al., 2015] that tend to intensify ground electric fields. At lower geomagnetic latitudes GICs can also be driven by interplanetary events such as coronal mass ejections (CMEs) and corotating interacting regions (CIRs) [Kataoka & Pulkkinen, 2008]. CMEs are the major causes of large GIC events [Hutturen et al., 2008], so the problem is fairly universal across a wide range of latitudes and time periods. Even within relatively uniform regional fields [Pulkkinen et al., 2015] there can be amplification of local peaks during severe GMDs [Ngwira et al., 2015] that increase the possibilities for significant GIC events that can be challenging to predict. For these reasons, researchers have actively investigated methods of mitigating GIC effects to protect power grids. Physically preventing the currents from entering power systems by adding series capacitors can harden sections of the grid against GIC-related damage, although doing so is expensive and tends to divert current to portions of the grid that are not protected, which can create GIC events downstream of the protected grid sections [Pirjola, Boteler et al., 2000].

GICs are often difficult to predict, so related factors have been considered as analogs to GICs with varying success, such as horizontal magnetic field changes [Viljanen et al., 2004; Weigel et al., 2002], solar wind patterns [Pulkkinen et al., 2007; Lotz & Cilliers, 2015], and ionospheric modeling [Pulkkinen et al., 2003; Viljanen, 1999]. These related techniques have mainly provided insight into GIC trends rather than being applied to operational predictions, though they have proved to be invaluable in building up GIC methods. There have also been examinations into past GIC events through the work of Wei et al. [2013] and Pulkkinen et al. [2005] to determine GIC causes and test how certain prediction methods would have worked if used at the time. Recent studies have been aimed at detecting GICs through means such as

solving coupled ionospheric and surface equations [Love & Swindinsky, 2014], vertical magnetic effects [Vanhamaki, 2013], and inversion [de Villiers & Cilliers, 2014]. These techniques have typically been accurate, although too slow and computationally intensive for direct application by industry.

Applied research efforts have been aimed at understanding the nature of GICs to predict and effectively mitigate them through dynamic control of the grid as an alternative to widespread hardening of transformers. GIC prediction software has been developed to model in near real-time the effects within a power system of changes in the electric field at ground level due to GMDs [Overbye et al., 2012; Khosravi and Johansson, 2015], so that voltages within the system can be biased to lessen harmful effects. The GIC prediction problem reduces the components of the specified grid to an equivalent complex circuit, and it uses the ground electric field along the components of the grid to determine the variable intensity of current flow in response to the imposed electric field [Pirjola, 2002]. This approach is already used within the power industry, but current practice is limited to applying electric fields associated with induction in a crust and mantle where the electrical conductivity is 1-D [Pulkkinen et al., 2007], i.e. it is permitted to vary only with depth. The Electric Power Research Institute (EPRI) has published a set of regional 1-D conductivity models [EPRI, 2012] that are employed for this purpose by industrial GIC prediction codes.

There is growing recognition that the electrical conductivity of the crust and mantle varies strongly in all three spatial dimensions [Kelbert et al., 2012; Meqbel et al., 2014; Schultz et al., 2014; Evans et al., 2014], and that 3-D conductivity variations can lead to significant intensification of ground electric fields [Thomson et al., 2005; Bedrosian and Love, 2015; Love et al., 2016]. Solutions to calculating ground electric fields in the time domain that are related to GMDs for the coupled ionospheric-Earth 3-D induction problem often employ

finite difference time domain (FDTD) solutions in massively parallel computing environments [e.g. Simpson, 2009]. At present such solutions are several orders-of-magnitude slower than real-time even on the largest available high performance computing systems. This presents a barrier to the industrial adoption of realistic 3-D ground conductivity models for purposes of GIC prediction. In contrast, solutions that follow current industry practice, based on 1-D regional approximations to ground conductivity, are sufficiently fast to be of practical use. The accuracy of such solutions hinges on the integration of the ground electric field along the path of a power transmission system, which might tend to average out 3-D effects, but the general suitability of this approach remains an open topic of research. In the present work we consider an alternative method by which non-uniform ground electric fields and their associated GICs may be determined rapidly and to reasonable accuracy when induced by GMDs above a 3-D Earth. We also address the inadequacy of the 1-D approximation for a real-world example of estimating ground electric fields.

While now embedded in industry practice, the compendium of regional-scale electrical conductivity models of the crust and mantle organized in the EPRI report is based on information that predates the widespread and systematic installation of magnetotelluric (MT) stations across the continental US through the support of the National Science Foundation funded EarthScope Program [Schultz, 2009]. Other large MT array data sets are also being acquired, or have recently been acquired elsewhere in the world [Jones et al, 2008; Thiel, S. et al., 2016], so the method reported in this work may be broadly applicable.

The MT method is described in more detail in Section 2 of this paper. The results of 3-D inversion of EarthScope MT data collected on a grid of stations separated by no more than ~70 km, and in some cases more tightly spaced, has revealed crust and mantle structure that varies laterally on local, regional and continental scales by more than three orders of

magnitude at any given depth [Evans et al., 2014; Kelbert et al., 2012; Meqbel et al, 2014; Schultz et al. 2014]. Most important for purposes of GIC prediction, the EarthScope 3-D conductivity images of the crust and mantle [e.g. Meqbel et al., 2014] bear little resemblance to the regional 1-D conductivity profiles contained with the EPRI report [EPRI, 2012]. This discrepancy between 1-D and 3-D images of conductivity structure has significant impacts on both the intensity and direction of ground electric fields and associated GICs that would arise during a given GMD.

2 Predicting Ground Electric Fields through the Magnetotelluric Impedance Tensor

Electrical conductivity models of the Earth's crust and mantle are usually obtained by inverse modeling of electromagnetic transfer functions that describe the relationship between the magnetic and electric fields at or near the Earth's surface. In the magnetotelluric (MT) method for generating such models, measurements of orthogonal vector components of the naturally occurring time variations in the electric and magnetic fields at ground level are obtained over a period of time. The duration over which the data are measured depends on the depth of interest for the study, since the depth of penetration into a conducting Earth of incident time-varying magnetic fields scales inversely with the frequency of the signal, so long-period magnetic field variations penetrate to greater depth than short-period variations. As the time-varying magnetic fields diffuse into the crust and mantle, electric fields are induced, converting some of the energy of the incident magnetic fields into electric currents, thereby progressively attenuating the down-going magnetic fields with increasing depth. At ground level, the time-varying magnetic fields are predominately of ionospheric (source current) origin, with a fraction of the energy associated with secondary magnetic fields that diffuse up to the surface from the induced electric currents. The time varying electric fields at ground level are predominately associated with the induced fields, which are related to the

inducing magnetic fields by the electrical conductivity distribution within the sub-surface. Frequency therefore serves as a proxy for depth, so the electric and magnetic vector component time series are transformed into the frequency domain through Fourier transformation, and a set of transfer functions that relate the field components to each other are obtained.

The most common form of transfer function used for magnetotelluric inverse modeling, the MT impedance tensor, is a frequency-dependent quantity that relates the orthogonal horizontal components of the electric fields to the orthogonal horizontal components of the magnetic fields at each measurement site,

$$\begin{pmatrix} \boldsymbol{E}_x^f \\ \boldsymbol{E}_y^f \end{pmatrix} = \begin{pmatrix} \boldsymbol{Z}_{xx}^f & \boldsymbol{Z}_{xy}^f \\ \boldsymbol{Z}_{yx}^f & \boldsymbol{Z}_{yy}^f \end{pmatrix} \begin{pmatrix} \boldsymbol{H}_x^f \\ \boldsymbol{H}_y^f \end{pmatrix} + \boldsymbol{U}^f, \quad \textbf{(1)}$$

where *E* represents the complex-valued Fourier coefficients of the electric field, *H* the complex-valued Fourier coefficients of the magnetic field, **Z** the complex-valued impedance, **U** the incoherent noise, *x* and *y* the north and east directions respectively, and *f* represents a given frequency. Written in this form, the impedance **Z** is a complex-valued frequency domain tensor that can be used to project the magnetic field variations (a vector of a given magnitude and direction) at a given location on the Earth's surface and at a given frequency into the corresponding variations of the vector electric field for that location and frequency [Telford et al., 1990].

MT data are typically obtained through deployments of a number of temporary observing stations. In order to obtain data that yield electrical conductivity information on crust and mantle structure to depths of ~10 km – ~350 km below ground level, MT impedances must be known over the frequency band of ~10^{-4} Hz – ~10^{-1} Hz. To achieve this, each MT station typically operates for 10 d – 30 d at a given location within the survey grid, depending on the

level of geomagnetic activity and the conductance of the upper crust, factors that can impact the generation and attenuation of MT signals. Once MT data of sufficient quality and duration have been obtained at each site, the station is moved to another location on the survey grid and the process is repeated.

The classical MT method assumes that ionospheric signal sources are sufficiently distant to be considered plane waves [Cagniard, 1953]. While the plane wave assumption is generally valid, it breaks down at high geomagnetic latitudes near the conjugate auroral ovals and beneath the ionospheric equatorial electrojet, so classical MT processing methods [e.g. Egbert & Booker, 1986] that are resistant to the influence of a mild degree of non-plane wave sources on the impedance estimation process are restricted to a broad range of mid-latitudes [Wait, 1962] and methods that accommodate persistent and energetic non-plane wave sources must be adopted for those other regions [Imamura & Schultz, 2015]. The resulting frequency domain MT transfer functions typically contain information within each frequency band that is gathered from a wide range of source (inducing) magnetic field orientations. The calculated impedance tensors therefore represent the scaling between source magnetic fields and the electric fields that arise in response to these magnetic fields. This scaling should be valid for any plane wave magnetic field polarization within the frequency bands for which impedance elements have been obtained.

For scenarios where the ground conductivity varies only with depth (i.e. a 1-D Earth), the diagonal elements of the impedance tensor are zero and the off-diagonal elements are of equal magnitude and opposite sign. In this case the horizontal electric and magnetic fields in the Earth that are induced in response to GMDs remain mutually orthogonal regardless of frequency, polarization of ionospheric source fields, or location within the observation grid. In contrast, for a 3-D conducting Earth all four elements of the impedance tensor may be non-

zero, the relative orientation of the electric and magnetic field vectors can be non-orthogonal, and the direction and intensity of the ground electric field can vary dramatically at different frequencies, for different source field polarizations, and at different grid locations within a survey region. In the 3-D situation, even a small change in the orientation of the ionospheric source magnetic field during the course of a GMD can produce potentially large changes both in the intensity and orientation of the resulting ground electric fields. This is not the case for a 1-D conducting Earth. Furthermore, ground electric fields resulting from a GMD of a given magnitude and source magnetic field orientation can be intensified substantially (by up to an order of magnitude) for the 3-D case relative to the 1-D case [Thomson et al., 2005; Bedrosian and Love, 2015; Love et al., 2016], and can vary dramatically in direction and intensity from one GMD to another since the time-frequency content of source field intensity and orientation is unique to each GMD. An important consequence of this is that no general linear scaling exists between the ground electric fields predicted from a GMD acting on a 1-D conductivity model, and those predicted from a 3-D model.

2.1 Electric field distortion and impacts on predicting electric fields from magnetic fields

The impedance tensor **Z** (Equation 1) is a linear filter that projects the magnetic field at a given site into the electric field at the same site, for any source polarization and for any frequency within the bands for which it is defined. The impedance tensor therefore contains all information necessary to undertake that local field projection, which *includes* but *is not limited to* all known information about the electrical conductivity structure within the range of depths of penetration associated with the frequency content of **Z**.

MT data have finite spatial resolving power, which is determined by the actual subsurface electrical conductivity structure, the spatial extent and inter-station spacing of the MT

measurement array, and by the frequency content of and statistical confidence limits on the MT transfer functions used in the inversion. At depths shallower than a critical depth determined by the subsurface conductivity structure and by the highest frequency data available, there is essentially no structural resolving power and the MT method becomes insensitive to the structural details, although it remains sensitive to the bulk conductance (vertically integrated conductivity) of those shallow layers. It is well known, however, that the electric field can be distorted at all frequencies by the presence of near-surface heterogeneities (i.e. fine-scale 3-D structure of arbitrary complexity that is too small to be resolved by the MT data). The effect of these shallow "scattering layers" is to change the scaling between electric and magnetic fields at a given site [Bahr, 1988], even when the magnetic field within a survey area is broadly uniform [Pulkkinen et al., 2015], and even if the underlying deep electrical conductivity structure is also broadly uniform or even 1-D. In addition to information about deeper electrical conductivity structure, the measured impedance tensor also contains information about such "static distortion" effects, which can vary from site-to-site independently of the underlying, deeper 1-D, 2-D or 3-D conductivity structure information that is also contained within the impedance tensor.

Prior to inverting **Z** to obtain a 1-D or a 2-D ground conductivity model, shallow 3-D static distortion effects are typically removed from the impedance tensor using one of a series of "tensor stripping" operators [e.g. Groom and Bailey, 1989; Jones, 2011]. The modified or stripped tensor is then used for inverse modeling of the ground conductivity structure, free from the complications of the surface scattering layer. In the Groom and Bailey formulation, the undistorted or *stripped* impedance tensor may be given by

$$\mathbf{Z}_m = g\,\mathbf{R}\,\mathbf{T}\,\mathbf{S}\,\mathbf{A}\,\mathbf{Z}_2\,\mathbf{R}^T, \tag{2}$$

where $\mathbf{Z}_m$ is the measured impedance tensor, g is the "site gain", which is a scalar, **R** is a rotation matrix, **T** and **S** are "twist" and "shear" tensors respectively, **A** is the "anisotropy" or "splitting" tensor, and $\mathbf{Z}_2$ is the undistorted or "stripped" tensor. The subscript for $\mathbf{Z}_2$ refers to Groom and Bailey's assumption that there is an underlying or regional two-dimensional structure with a principal electrical strike direction beneath the distorting 3-D surface layers. The rotation matrix acts to align the undistorted matrix with the principal axes of that 2-D structure.

While this process has proven essential for 1-D and 2-D inversion for ground conductivity, there are differing opinions about the necessity of removing the distorting effects of unresolvable, shallow 3-D scattering layers prior to inversion of impedance tensors in fully 3-D environments. Methods have been developed for distortion removal [e.g. Utada and Munekane, 2000] prior to 3-D inversion, whereas others allow for shallow 3-D scattering layers in their 3-D models [Kelbert et al., 2012] that, while containing model cells that fall far below the resolving limits of the MT data set, may be used to express the galvanic distortion effects on the electric field.

The concept of tensor stripping has an important consequence for those applying ground conductivity models to the GIC prediction problem. Methods that solve for the ground electric fields given a known conductivity model that have first stripped out the effects of the shallow 3-D scattering layer (which is generally the case for published 1-D and 2-D models, and can be the case for some 3-D models) will produce *undistorted* ground electric fields, with the effects of static distortion removed. Such electric fields differ from those actually measured at each site, since the real-world electric fields *are* distorted by fine-scale heterogeneities in near-surface conductivity structure, whereas the MT-derived conductivity models typically have such effects removed. Efforts to use ground conductivity models based

on tensor stripped impedances will yield ground electric field predictions that will not, in general, match the measured electric fields on the ground. This point is not generally recognized in the GIC prediction literature.

Efforts to empirically adjust ground electric field predictions, such as those based on regional 1-D ground conductivity models, by calculating a heuristic scaling factor to minimize the misfit between observed and calculated GICs are essentially equivalent to efforts to estimate g, the site gain factor in Equation (2), independent of the other distortion tensors. By disregarding the other distortion factors, such an approach cannot adequately account for the rotation, shear and twist effects on the electric field due to the shallow 3-D scattering layers, which are ubiquitous even when the deep underlying structure is not 3-D. Since the electric field is a vector field, disregarding either shallow 3-D distortion effects, or deeper 3-D crust and mantle conductivity effects, or both, can significantly bias both the magnitude and the direction of the resulting ground electric field.

For the work reported here, based on using unstripped impedance tensors, these issues are not a factor. It is also not a factor when using 3-D electrical conductivity models to predict the ground electric field for the subset of 3-D models developed using unstripped impedance tensors and where a shallow galvanic scattering layer is an explicit component of the model, as opposed to those 3-D models that lack this layer and that are derived from inversion of stripped impedance tensors.

2.1 Projecting the contemporary magnetic field on to previously occupied MT measurement sites

For operational GIC prediction, the magnetic fields must be known at multiple points along the path of the power distribution system in near real-time, whereas the MT stations used to estimate **Z** at a set of locations are, in general, no longer operating, nor situated directly along

power line paths. While it is common practice in GIC research to apply a simple geomagnetic latitude scaling factor to represent the geographic dependence of GMD magnetic field intensity, we propose a different approach. We hypothesize that magnetic fields recorded by magnetic observatory networks, such as those operated by the US Geological Survey (USGS) or equivalent agencies around the world, can be projected on to the locations of previously occupied MT stations by construction of frequency domain transfer functions that relate the magnetic field variations at one or more magnetic observatories to the magnetic field variations that were actually recorded at each of the MT observation sites during the same period of time. We further posit that once determined, the transfer functions can be used to project real-time magnetic field variations data from those observatories into real-time predictions of the magnetic field at each of those sites. The MT impedance tensors associated with each site (which contain all known information about 3-D conductivity structure beneath and surrounding those sites, including shallow distortion/surface scattering effects) can then be used to project the real-time predictions of the magnetic fields at those sites into real-time predictions of the ground electric fields. These can then be interpolated from the MT station locations onto the locations of the power distribution lines.

The MT data necessary to test this hypothesis were collected from a temporary MT array spanning western Oregon and southwestern Washington, shown in Figure 1, under the support of a National Science Foundation (NSF)-funded joint EarthScope-GeoPRISMS project EAR-1053632, "Onshore-offshore MT Investigation of Cascadia Margin 3D Structure, Segmentation and Fluid Distribution", along with magnetic observatory data collected by the USGS. Electric field components at the MT array sites were determined from geomagnetic north-south (x) and east-west (y) oriented 100-meter long dipoles that consisted of cables linking pairs of grounded Pb-$PbCl_2$ electrodes, and the magnetic field components were measured via sensitive, observatory quality Narod Geophysics triaxial ringcore fluxgate

magnetometers that were oriented toward geomagnetic north. Narod Intelligent Magnetotelluric Systems (NIMS) recorded time series of each of the electric and magnetic field vector components at one-second intervals. The effects of local cultural electromagnetic noise on the measured impedance tensors was reduced through remote reference processing [Gamble et al., 1979]. Short data gaps were removed, and the influence of non-stationary and non-plane wave signal sources was minimized using methods enumerated in Jones et al. [1989] and Egbert & Booker [1986].

In contrast to the temporary MT array data, magnetic observatory data are collected continuously and adjusted for baseline shifts due to instrument drift, whereas temporary MT station data are collected for a limited time period and do not adjust for such shifts, thereby restricting the usable frequency bandwidth to a practical low frequency limit of ~10^{-4} Hz in most cases. This restricts the sensitivity of the MT data to mantle depths of ≲350 km below ground level. If the need arises, deeper conductivity information can be obtained using other methods [e.g. Kelbert et al., 2009], although these provide 3-D information of lower spatial resolution than MT based results.

A hallmark of MT data obtained under NSF EarthScope support is its availability to the general public without restriction [Kelbert et al., 2011], the provision of pre-calculated impedance tensors as well as time series, and the geographic scope of the EarthScope MT Program (Figure 1) with a grid of stations with nominal 70 km station spacing. In some cases, higher resolution MT data with closer station spacing (such as that shown in Figure 2) exists separate from the EarthScope MT Transportable Array shown in Figure 1. The EarthScope Program ends in 2018, and additional MT stations will supplement those shown in this figure in the intervening time, with plans to extend the southern extent of the array that currently covers the north-west quadrant of the US, by adding 2-3 rows of stations, and with the

possibility of a sparser array of sites to be installed in the Great Plains to bridge the two large existing MT arrays seen in the figure. By the conclusion of the EarthScope Program, half of the area of the continental US will be covered by long-period MT data.

The wide geographic scope of these open-access data sets opens up the possibility that the method demonstrated in the present work can be broadly applied across the territory of the US, and in areas where other large-scale MT array data exists, more globally as well. In areas where no such MT data exist, it is feasible to expand upon the existing EarthScope MT array to acquire MT impedance tensor information in areas of interest to the electric utilities.

3 Algorithmic considerations

Electric field predictions along the path of a transmission line can be generated by projecting a real-time stream of magnetic observatory data through observatory-to-MT site magnetic field transfer functions, and then by projecting the resulting predicted magnetic fields at each of the previously-occupied MT stations through the impedance tensors calculated from previously collected EarthScope data. Doing so produces electric field predictions at the corresponding (former) MT measurement sites, which can then be interpolated from the MT array locations onto points representing the transmission line. The values of the vector ground electric field for each of these points can then be integrated to obtain the total ground electric field along the line, which is necessary for GIC calculations and damage mitigation. The data flow from magnetic observatory data to total electric field predictions is shown below in Figure 3.

The first step involves determining a transfer function for each MT station whose input signals consist of the vector magnetic field variations recorded at one or more magnetic

observatories, and whose output signals are the vector magnetic field variations that were actually recorded during the operation of each MT station. The observatory and MT station time series must be synchronous and concurrent, with identical sample intervals. Accuracy is improved when nearby observatories are included that surround and effectively bound the MT station array.

For the example reported here, utilizing MT array data that spans much of western Oregon and southwest Washington in the United States (Figure 2), the USGS magnetic observatories chosen were Newport Washington, Boulder Colorado, Fresno California, and Honolulu Hawaii. The closest observatory, Newport, lies approximately 540 km from the center of the MT station array, whereas Honolulu, the most distant observatory, lies approximately 4,150 km from the center. While geographically favorable, data from the magnetic observatory at Victoria, British Columbia, Canada were not used since a real-time data stream of 1-sample per second data is not currently available from that site, whereas an open source library of Python language [Van Rossum, 2003] scripts have been developed by the USGS Geomagnetism Program [Geomag Algorithms, 2016] that make such data accessible in (near) real-time from the USGS magnetic observatory network.

Multi-station transfer functions that relate the magnetic field vector components at the set of observatories to the magnetic field vector components at a given MT station were obtained following the algorithm of Zhang and Schultz [1990]. The frequency domain transfer function $\Gamma(\omega)$ that relates data at a local MT station simultaneously to data at a set of one or more remote observatories is given by

$$X_o(\omega) = \sum_{i=1}^{M} \Gamma_i(\omega) X_i(\omega) + \delta X(\omega), \quad (3)$$

where $X_0(\omega)$ and $X_i(\omega)$ $(i \neq 0)$ are the complex-valued Fourier coefficients of the local and remote components of the vector magnetic fields, ω is the radian frequency ($\omega = 2\pi f$, where f is in Hz), $\delta X(\omega)$ is the uncorrelated residual, $\Gamma_i(\omega)$ is a partial transfer function relating X_0 to X_i, and M is the number of remote observatories. The solution for $\Gamma(\omega)$ is found by minimizing the L_2 norm of the residual $\delta X(\omega)$ for each frequency band

$$\min [\![\delta X(\omega)^2]\!] = \min [\![\left|X_o(\omega) - \sum_{i=1}^{NxM} \Gamma_i(\omega) X_i(\omega)\right|^2]\!], \quad (4)$$

where the brackets $[\![\ ]\!]$ represent a frequency band-averaging operator, and Γ is taken to be invariant within each frequency band. We solve for the transfer function coefficients by QR decomposition of the normal equations. In practice, the calculation of the transfer functions is an iterative process, where in each iteration the residual between the predicted magnetic field at each MT station location is calculated from

$$\delta x_0(t) = x_0(t) - \mathrm{FFT}^{-1}[\sum_{i=1}^{M} \Gamma_i(\omega) X_i(\omega)], \quad (5)$$

where the inverse Fast Fourier Transform (FFT^{-1}) operator [Cochran et al., 1967] yields a time domain prediction of the magnetic field components at a given MT station location from the Fourier coefficients of the magnetic field components at the remote magnetic observatories as projected through the transfer function, and where $\delta x_0(t)$ is the residual between that predicted field component and the measured field component $x_o(t)$ in the time domain. When the magnitude of the residual exceeds a certain threshold, taken by Zhang and Schultz [1990] to be a multiplicative factor of the interquartile deviation around the median value of all residuals, the data point is taken to be an outlier and it is replaced by the predicted

value. The process iterates until no additional outliers are detected, as described in more detail in Zhang and Schultz.

Prior to transformation to the frequency domain, short gaps in the time series are interpolated by autoregressive prediction [Janssen et al., 1986; Zhang & Schultz, 1990], and the time series is high-pass filtered to remove energetic diurnal variations typically associated with ground electric and magnetic fields that cause spectral leakage and drift [Stearns & Hush, 1990]. This drift biases the predicted signal and can introduce step discontinuities between adjoining sections of predicted data. The windowed data are then prewhitened by removal of the mean value and the best-fitting linear trend, then the data section is multiplied by a time domain taper function to minimize spectral leakage between frequency bands. We apply a time-bandwidth product 4 prolate spheroidal taper function [Chave & Thomson, 2004] for this purpose. A data window length is selected that is sufficiently long to contain multiple cycles of harmonic signals matching the lowest frequency band found in the MT transfer functions, which is typically 10^{-4} Hz. A minimum of ten, and ideally as many as one-hundred or more 10,000 – 20,000 s long sections of time series data is required in order to achieve a statistically acceptable frequency domain representation of these low frequency signals. Examples are shown later using differing window lengths within this range. As is the case generally for Fourier analysis, it is assumed that the signal is stationary within the time window selected. While the examples shown later suggest the assumption of stationarity leads to excellent predictions, the method introduced here could be refined by applying time-localized analogs to the FFT, such as wavelet or the *S*-transforms [Yun et al., 2013], although this is outside the scope of the present work. Other details of the iterative refinement of the transfer function estimates can be found in Zhang & Schultz [1990].

3.1 Interpolating predicted fields onto the power transmission grid

The next step in preparing for real-time predictions involves interpolating ground electric field data from the MT station sites onto points along the path of nearby transmission lines. We make use of a nearest neighbor interpolation algorithm following Schultz & Pritchard [1999]. We construct a Delaunay triangulation [Chew, 1989] of the MT station locations (as seen previously in Figure 2), where the MT station locations are the vertices of the triangles. We determine if a given point along a transmission line path is contained within the convex hull of each Delaunay triangle, which is true if the determinant of the point and each vector comprising the triangle is positive i.e. the point is to the left of each side when going in a counter-clockwise direction [Barber *et al.*, 1996]. We determine the great circle distance between each point along the path of the transmission lines and each vertex of the Delaunay triangle that contains the given point. Once the ground vector electric field variations have been predicted at the vertices (each of which is the location of a previous MT station and impedance tensor estimate), the electric field is interpolated onto the transmission line path by averaging the vector electric field values at the three vertices of the Delaunay triangle that encompasses that point, weighted inversely by the distance of each vertex from that point along the transmission line path.

This approach contrasts with methods that directly apply an existing electrical conductivity model of the crust and mantle to the problem of predicting ground electric fields by solving the forward problem of electromagnetic induction for a given source field model in either 1-D, 2-D or 3-D. The primary difference in approach is that the forward solutions obey the governing equations for electromagnetic induction, whereas our strictly geometrical, nearest neighbor interpolating function does not. On first glance this would seem to be a significant

disadvantage to our approach, but one must consider the intrinsic inaccuracies and approximations that go into solving the electromagnetic induction inverse problem to generate a conductivity model. At each point within such a model, the conductivity is discretized to a certain degree, it is known to a given uncertainty, and rather than representing an exact point estimate of the true conductivity at each location, it is a volume-averaged estimate of the conductivity whose spatial averaging function is difficult to establish given the nonlinearity of the inverse problem. Ultimately such a conductivity model represents a series of propagated uncertainties at every step of fitting the observed impedance tensor (and, potentially other data as well). As mentioned previously, that model may also omit surface scattering layers that can have a profound impact on the electric field at all frequencies.

In our approach we avoid solving the electromagnetic induction problem and instead consider the impedance tensor strictly as a linear filter that transforms ground magnetic fields into ground electric fields. Since this skips the steps of solving an electromagnetic induction forward problem for a discretized model, we believe there are fewer opportunities for errors to be introduced in the projection of magnetic fields to electric fields at each MT station location. It is an open question whether the next step, the interpolation of predicted ground electric fields onto the transmission line paths, introduces greater errors than the accumulated errors of solving the induction forward problem based on a conductivity model of finite discretization and uncertainty. It is also an open question if there will be a systematic bias from interpolating electric fields that contain local static distortion effects onto the path of the transmission lines, since such distortion may be local to each point along the path. It may transpire that this fine-scale distortion will average out as the ground electric fields are integrated along the transmission line path for purposes of predicting GICs. While we do not have definitive answers to these questions at present, our initial results, provided below,

suggest that the geometric interpolation of distant magnetic observatory data through successive transfer functions and impedance tensors is an effective approach.

4 Results

The fundamental problem we address in this work is the near real-time prediction of electric fields along the path of power distribution lines without the computational burden of explicitly solving the coupled equations for electromagnetic induction above a known Earth conductivity model. To accomplish this, we employ a set of previous recordings of electric and magnetic fields and previously calculated MT impedance tensors at an array of MT station locations that encompasses the powerline pathway. By successively applying a set of linear filters (first a transfer function that relates distant magnetic field observations to those previously recorded at the MT stations, and then a set of MT impedances that project the local magnetic field variations into local electric field variations), we seek to show that we can faithfully reproduce the magnetic and electric fields that were actually recorded at the MT stations. Having accomplished that, we then seek to show we can reasonably interpolate the predicted electric fields to any location within the geographic span of the MT array, which would include the paths of the power distribution system of interest. We refer to our approach subsequently in this work as the "Cascading Linear Filter Algorithm", or CLFA.

In this section of the paper, we demonstrate the contributions to the prediction of the electric field variations from each aspect of the CLFA prediction process. First, we examine the impact that distance between the local MT station location and the distant magnetic observatories has on the integrity of the predicted local magnetic fields. We then demonstrate the effectiveness of using such predicted local magnetic fields to generate predictions of the local electric fields by projecting the magnetic fields through the local MT impedance

tensors. Finally, we demonstrate that we can use the nearest neighbor interpolation method described in Section 3.1 to project a set of predicted electric fields from MT station locations surrounding a point of interest and faithfully reproduce the electric field actually recorded at that point.

4.1 Projections of magnetic fields from a single distant observatory to a single MT station

To start, we construct a set of simple transfer functions that project the magnetic field components at a single distant magnetic observatory to those at a single MT site, i.e. we set $N = 1$ in Equation (3). Figure 4 displays the individual projections of the magnetic field from each of the four magnetic observatories used in this study through such single station transfer functions, which yields a set of four different predictions of the local magnetic field at the given MT site. This illustrates that the proximity of the magnetic observatories impacts the quality of the fit between observed and predicted magnetic fields. The projected magnetic fields from the closest observatory at Newport, Washington best match the actual magnetic fields at the MT station (designated site G012, located 50 km northwest of Portland, Oregon and ~500 km from Newport, Washington), due to the high coherence between the two signals. The coherence between the magnetic fields decreases with greater station separation, in part because of spectral leakage from long-period signals such as diurnal variations that have increasing phase and magnitude difference with increasing distance. Differences aside, by employing multiple remote magnetic observatories (setting $N = 4$ in Equation (3) in this case) improves the overall fit of the predicted magnetic field relative to the single station case. This will be illustrated in subsequent examples. Observatories with higher coherence with the local signal have a larger impact on the fit of the predictions, which can be problematic if errors in the real-time stream of data from these observatories go undetected

during real-time predictions, yet the inclusion of other observatories does improve the fit of the projected magnetic fields.

We also examine the effect of increasing magnetic observatory distances on the quality of the predicted electric field at an individual MT station (Figure 5). As is expected, electric field prediction quality degrades with distance as magnetic field prediction errors are propagated through the impedance tensor. Figure 5 demonstrates the distance limitations in using only a single distant observatory for electric field predictions. Panels (A) and (E) in Figure 5 show the north-south (x) and east-west (y) recorded and predicted electric fields based on projecting the magnetic fields from relatively nearby Newport observatory, at a distance of ~500 km from the station, over a time period of ~11.6 days. Viewed on this scale, aside from a short duration event at about 550,000 s from the start of this record, the predicted and recorded electric field components conform to within a couple of mV/km, or less. More quantitative analysis of the prediction misfits arising from using multiple rather than single observatory data sets will follow, but this serves to illustrate the point that observatory distance impacts the fidelity of the electric field predictions. Panels (B) and (F) for data projected from Boulder (1546 km from site G012), (C) and (G) from Fresno (1004 km), and (D) and (H) from Honolulu (4175 km) show progressively increasing prediction misfits with distance. At the greatest distances electric field prediction misfits are more typically in the 5-10 mV/km range.

4.2 Projections of magnetic fields from multiple distant observatories to a single MT station

Improvements in predicting the magnetic field components at each MT site by simultaneously projecting magnetic fields from four remote magnetic observatories (i.e. setting $N = 4$ in Equation 3) can be seen in Figure 6, where the coherence between the measured and predicted time series is apparent, even when viewed in more detail on a much finer time scale (*x*-axis) and field amplitude scale (*y*-axis) than shown previously in Figure 4. Given the fine scale of this plot, we show the projected magnetic fields with ±95 confidence intervals, where the magnetic field transfer function covariances are calculated by adapting Eisel and Egbert's (2001) basic transfer function covariance expression (their equation [11]) to the multiple station magnetic field problem, following which we propagate the uncertainty in the transfer function into the projected magnetic fields by applying classical uncertainty propagation theory (Ku, 1966). Minor deviations still remain due to limitations with the algorithm, such as the need to group the frequencies into a small number of bands that smooth out the energy contained within any narrow-band spectral peaks that might be encountered.

The conditions that produced the lowest misfit predictions, shown in Figures 6 through 11, included using a moving 20,000 s data section window tapered by multiplying by a time-bandwidth product 4 prolate spheroidal taper function with 50% overlap between adjacent time series sections to estimate the Fourier coefficients used for calculating transfer functions and for projecting the remote data to obtain the local predictions. The data were also high-pass filtered using a four-pole Butterworth filter with a corner frequency of 10^{-4} Hz prior to Fourier transformation into the frequency domain, to best match the frequency bandwidth of

the MT transfer functions typically available for EarthScope MT stations (~10^{-4} Hz – 10^{-1} Hz, or 10 s to 10,000 s period).

4.3 Projections of local magnetic fields through the MT impedance tensor

The final step in the CLFA process of predicting the local electric field variations at each MT station involves projecting the predicted magnetic fields for that location through the local MT impedance tensor. Any deficiencies in the projected magnetic fields at that site (which could contain signal components that are non-stationary and that may be contaminated by non-plane wave sources such as artefacts of cultural noise) through an impedance tensor that may itself contain a degree of error, could degrade the fidelity of the resulting predicted electric field.

As a first step, we examine the quality of the electric field prediction that would result from projecting the magnetic fields actually recorded at the MT station through the local impedance tensor. In principle such a predicted electric field should closely match the recorded field, since the recorded fields were used to estimate the impedance tensor. The purpose of this exercise is to demonstrate what portion of the original signal is not adequately modeled by the impedance tensor, which is a linear filter estimated by assuming the source signal is a stationary plane wave, and that down-weighted the influence of data sections that violated that assumption. The result is seen in Figure 7.

Figures 6 and 7 both show high coherence between measured and predicted magnetic and electric field components, respectively, although the smaller uncertainty in the predicted electric fields in Figure 7 relative to the uncertainty in the predicted magnetic fields in Figure 6 reflects the larger uncertainty in the multiple station magnetic field transfer function

relative to the uncertainty in the local impedance tensor estimate. This likely reflects more complex noise structures and lower coherences between magnetic fields at sites separated by many hundreds-to-thousands of km relative to the purely local electric and magnetic field relationships at the magnetotelluric station. Aside from some long-period drift and scaling issues that are occasionally present in the field predictions, the multiple station transfer function based prediction filter, and the local impedance tensor prediction filter are demonstrated to adequately replicate the measured data at the MT sites within the frequency range for which the impedance tensor is known.

4.4 Projections of predicted magnetic fields through the MT impedance tensor

Projecting the magnetic field at the four remote magnetic observatories through the multi-station transfer function, and then projecting the resulting predicted magnetic field at the MT station through the local impedance tensor leads to the electric field predictions shown in Figure 8. This series of steps constitutes the full CLFA prediction process. These results can be contrasted with Figure 7 to gauge the impact of projecting predicted vs. actual magnetic fields through the impedance tensor. The predicted electric field components at the MT site retains high coherence with the electric field components actually recorded at the site despite the minor compounding misfit introduced from the magnetic and electric portions of the prediction process that were shown previously, of which the propagated uncertainty in the magnetic field prediction is the dominant contributor. Misfits appear to scale with the magnitude of the signal, which is demonstrated most clearly in the E_y prediction. Overall, we found that our prediction algorithm produces low electric field prediction misfits at most sites that are typically around 1– 2 mV/km RMS, aside from the occasional outlying peak or interludes of reduced coherence that appear as phase shifts or noise. High coherence and low

misfit are retained for the great majority of 10,000 s time series sections at multiple MT sites that we have examined.

4.5 Nearest neighbor interpolation of ground electric fields

In Section 3.1 above, we described our algorithm for distance-weighted interpolation of the predicted ground electric field vector components from a set of MT stations that most immediately surround a given point along the path of a power transmission line. While in the present work we can provide no examples within our MT station array of electric fields as actually measured along a transmission line, we illustrate the effectiveness of this interpolation method by carrying out a Delaunay triangulation of our MT array (Figure 2) with a single station location deleted, and then interpolating on to the location of that missing station the electric fields predicted using the CLFA method from the three MT station locations most closely surrounding it. We compare these interpolated electric field components with the CFLA prediction of the electric field calculated for that site.

For this purpose, we require a set of three MT stations that form a Delaunay triangle that encloses a fourth station, all of which recorded electric fields simultaneously for a considerable period of time. The station combination C013, C015 and D013 (Figure 2) met this condition and serve as the vertices of the enclosing Delaunay triangle around station C014. (The Delaunay triangles shown in Figure 2 are for the complete set of all MT stations in the array, and do not show the new Delaunay triangle that connects stations C013, C015 and D013 once station C014 is omitted from the array.) Figure 9 shows the result of the nearest neighbor electric field interpolation for a time series section, displayed on a fine scale of ~1 d time duration and over a ±3 mV/km range. As indicated previously it is still an open question whether local electric field distortion at each site will inevitably degrade the fidelity

of the geographically interpolated fields, introducing potentially larger errors than alternative approaches based on the forward solution for the electric fields above a model of known conductivity. In the present example, where the distance between local station C014 and the interpolating stations ranges between 11 km – 16 km, and all sites lie within a similar geologic setting, nearest neighbor interpolation of the predicted electric fields matches the site prediction of the electric fields to within a fraction of a mV/km aside from brief excursions of O(1 mV/km) specifically in the E_x component. This discrepancy is smaller than the typical misfit between predicted and measured electric fields reported earlier (Figure 8) so lies within the margin of error.

The example shown above where the distance from the interpolating point to the most distant MT station does not exceed 16 km reflects the augmentation of the EarthScope MT Transportable Array, with nominal 70 km MT station spacing (Figure 1), with a much finer station spacing of the EarthScope-GeoPRISMS special study area MT array in western Oregon and southwestern Washington (Figure 2). More typically, where EarthScope MT data exist, it is on the ~70 km station spacing grid seen in Figure 1, which could lead to a maximum distance from the interpolating point along a power transmission line path and an EarthScope MT station approximately three times greater than the example shown here. We have repeated all steps shown above to predict and project electric fields for a more typical ~70 km EarthScope MT array for a power transmission line in Wisconsin and Michigan. While the results are not shown here (they will be the subject of a subsequent paper), we can report that the degradation in fidelity of the interpolated electric fields is very modest and within the confidence limits of the predicted electric fields at the MT station locations.

4.6 Comparing our results to those generated from 1-D conductivity models

Our CLFA electric field predictions can be compared to those generated by following the North American Electric Reliability Corporation (NERC) guidelines outlined in [NERC, 2013]. Rather than constructing a series of cascading linear filters as we have done to project the magnetic fields measured at multiple magnetic observatories to the location of interest and then projecting the resulting predicted magnetic field through the local MT impedance tensor, the NERC guidelines directly employ the magnetic field data from the nearest USGS magnetic observatory as representative of the magnetic field at the local site. The NERC guidelines then call for solving the electromagnetic induction problem for the predicted electric fields above a known 1-D Earth conductivity profile, given the magnetic observatory magnetic field data as input. There do not appear to be any set NERC standards for specific window type, window length, filtering level, or various other parameters, so the same values that we used with our method were used for consistency. We solved for the 1-D impedance at the same set of frequencies at which EarthScope 3-D impedances are calculated, but for the 1-D electrical conductivity model found in the EPRI [2002] PB-1 conductivity map that represents the area containing our MT array.

Figure 10 displays a direct comparison at MT station G012 (see Figure 2) between the NERC electric field time series predictions, our CLFA based predictions, the original time series, and a hybrid method where our (linear filter) predicted magnetic field was instead projected through the EPRI [2002] 1-D model impedance rather than through the (3-D) EarthScope impedance tensor for that site. By presenting the results of the hybrid method in comparison to the CLFA results, we eliminate any variation due to differences in the magnetic fields used for the calculation and instead illuminate the differences attributable solely to using 1-D vs. 3-D ground conductivity information. Figure 10 also displays a comparison between these

various predictions but for a much longer time period, which is displayed as RMS misfit between the recorded and predicted electric fields, binned into 6-hour intervals.

The first thing to note is that our linear filter prediction method generates values that better match the electric field time series that were actually recorded at the MT stations, with lower misfit across all time scales (Figures 10 and 11). While we show examples from MT station G012, this statement is true at all stations that we have examined within the MT array shown in Figure 2. This difference is more clearly demonstrated in E_x than in E_y at MT site G012, which can be explained by the strongly 2-D nature of the electric conductivity structure beneath that location. For 2-D electrical structure, the impedance tensor can be rotated into the direction of geoelectric strike, where impedance tensor element $Z_{x'y'}$ (Equation 1) represents the transverse electric (TE) mode where the electric field is parallel to strike and $Z_{y'x'}$ represents transverse magnetic (TM) mode where the electric field is perpendicular to strike. The primed subscripts refer to the rotated coordinates, where *x*' is aligned with strike direction. TE and TM mode impedances exhibit different sensitivity to the presence of higher dimensional structure. For the present example, the E_x component of the predicted field is highly sensitive to the presence of 2-D and higher dimensional ground electrical structure, whereas the E_y component is less so. As a consequence of this, the electric field prediction based on the NERC guidelines does a particularly poor job of fitting the E_x electric field that was actually recorded at site G012. The short timescale NERC guideline based predictions of E_y match the high frequency variations in the E_y time series recorded at the site (Figure 10), but there are significant peaks, troughs and longer period changes that are completely missed in the predicted E_x component.

The quality of predictions for both E_x and E_y obtained following NERC guidelines would likely degrade more severely in the presence of highly 3-D conductive structures, since there

would be no preferred geoelectric strike direction, and higher dimensional effects would be seen strongly in both electric field components. This is also the case for predictions based on the hybrid method. In both cases we have found that the impact of higher dimensional ground conductivity structure on the degradation of ground electric field predictions is the dominant source of error in the predictions, rather than the modest differences in the quality of the predicted magnetic field. Our proposed CLFA linear filter prediction method accommodates higher dimensional ground conductivity structure implicitly, and is better able to match the electric field data actually recorded at the MT stations.

The same trends over the 10,000 s time series section displayed in Figure 10 are also observed for time series sections up to and including 10^6 s long (the longest section we have examined). Since it is difficult to clearly display such a large number of points to visualize the details of the misfit, over each interval of 6-hours we have calculated the RMS misfit between the measured electric field components at MT site G012 and the predicted electric fields at that site, according to

$$RMS = \sqrt{\frac{1}{n}\sum_{i=1}^{n}(site_i - pred_i)^2} \ , \qquad (6)$$

where $site_i$ is the measured field and $pred_i$ is the predicted field. This is seen for a 10^6 s time series section in Figure 11.

As would be expected from the previous comparisons, the RMS misfit between recorded and predicted electric fields is fairly similar for the E_y component from all three prediction methods, whereas for the E_x component (which is more influenced by non-1-D electrical conductivity structure than E_y in this case), our cascading linear filter algorithm has much

lower RMS misfit than either the NERC method or the hybrid method. In particular, electric field predictions from the NERC method can misfit the electric fields actually recorded at the MT station locations by several hundreds of percent more than those calculated using the CLFA approach. This is evidence that methods that employ 1-D ground conductivity models have noticeable limitations on accuracy outside of those atypical locations where ground conductivity structure is approximately 1-D.

One of the rationales for applying the NERC guidelines, which employ 1-D models of ground conductivity rather than the more complex data-based 3-D impedances used in the CLFA approach, is that 1-D methods are still capable of reliably estimating peaks in GMD induced ground electric field intensity that would actually cause or indicate GIC events, so the degree of mismatch on smaller fluctuations is unimportant. Figure 11 demonstrates that this reasoning is questionable for locations with heterogeneous (2-D or 3-D) electrical structure. The EarthScope MT program has revealed that highly 3-D structure is ubiquitous throughout all regions that have been instrumented (Figure 1), which currently comprises nearly half of the territory of the continental US (including the Pacific Northwest area that serves as our testbed for this paper). It is premature to conclude anything about the effects of these discrepancies on predicting actual GIC events, particularly since the act of integrating ground electric fields along power line paths could reduce the impact of 3-D variations, at least for certain geographic settings and power distribution topologies, yet it does seem clear that by disregarding the 3-D information contained in MT impedance tensors and basing ground electric field predictions on 1-D models, significant inaccuracies can result.

5. Discussion

The main limitation apparent from these examples is the need to use a high-pass filtered version of the site time series to assess fit since long-period signals outside of the frequency band for which the impedance tensor is known (such as diurnal variations in the electric and magnetic fields) would otherwise leak energy into the frequency bands of interest, thereby introducing long term drift that could degrade the predictions.

One method of resolving this issue would be to extend the MT impedance tensors to lower frequencies in order to capture diurnal variations. This is problematic, since for the case of EarthScope and similar temporary campaign-style MT investigations, the finite duration of the data set limits the lowest frequencies to the values already achieved. While there are a limited number of EarthScope MT stations that were specifically designed to obtain MT impedance data to frequencies as low as 10^{-5} Hz, it is technically very challenging to obtain stable electric field measurement at such low frequencies, so these were exceptional installations and do not provide a general solution to this issue. Another approach is to make use of deeper, global-scale 3-D mantle conductivity models that have been obtained through methods involving analyses of magnetic field data exclusively [Kelbert, et al., 2009; Sun, et al., 2015]. While having effectively no spatial resolving power in the upper ~350 km of the crust and mantle, these models typically describe deep Earth conductivity variations for mantle depths of ~350 km – ~1200 km in terms of an underlying radially symmetric (i.e. 1-D model) compromising a series of radial shells of finite thickness, with 3-D variations in conductivity represented as a set of spherical harmonic coefficients about the underlying baseline model. By solving the forward problem for 3-D induction for such a model, a set of equivalent MT impedance functions could be generated at the MT station locations to provide the lower frequencies that otherwise are absent from the EarthScope impedance tensors. By appending these ultralow frequency impedances to the MT impedances, this could provide

predictions free from the minor long-period drift issues we sometime encounter, which would generate even closer real-time total electric field predictions and thus improve GIC mitigation.

The cascading linear filter algorithm (CLFA) we have demonstrated, making use of 3-D information implicit in the impedance tensors, reproduces ground electric fields with greater fidelity than the NERC guidelines approach or the hybrid approach, and its computational demands are very modest. To gauge the suitability of the CLFA code for operation in industrial settings with modest computing infrastructure, we have tested the algorithm on an obsolete desktop computer with an Intel® Celeron® G1610 (2.60GHz) processor, 4 GB of DDR3 SRAM, under the MS Windows 8™ 64-bit operating system, and find that predicting electric field values given a 100,000 s section of magnetic observatory data takes ~1 s to run on such a computer. Minor efficiency improvements and parallelization of series components of the code, or simply running it on a faster computer would speed computations to a fraction of a second, enabling true real-time ground electric field calculations. Internet latency and throughput can be a consideration in maintaining real time electric field prediction capabilities. In our experience there is a 10-15 s latency between requesting data from the USGS servers and receiving it through the Internet regardless of the length of the data set requested, even when using hard-wired internet connections that otherwise are able to maintain gigabit per second speeds to distant servers.

While a delay of up to 15 s might not pose a serious problem for operational GIC prediction, in the event true real time throughput is needed, a small array of observatory quality magnetometers could be installed at sites close to the power grid to transmit data through dedicated telemetry links. In addition to reducing the latency of obtaining magnetic field data,

the fidelity of the electric field predictions along the power line path would likely improve given the decreased distances involved. Nearby magnetometers could also provide estimates for local noise, which is important to the electric field but neglected at present.

Combining all of the suggestions would likely further improve ground electric field predictions, GIC mitigation and power grid safety, yet the current estimates based solely on distant magnetic observatory data still appear to be useful even without. This bodes well for integrating the output of our real-time algorithm and its output of non-uniform electric fields as the input into industrial GIC prediction software. The next step in this research effort is to carry out such integration with industrial GIC prediction software, which we plan to do after we complete additional improvements to long-period ground electric field predictions.

6. Conclusions

A new cascading linear filter algorithm (CLFA) for accurately predicting the horizontal vector components of ground electric fields in real time, needed for predictions of geomagnetically induced currents (GICs) was described, tested for numerical and methodological validity, and examined for potential issues or improvements. The CLFA method projects the horizontal vector components of the magnetic field variations at a set of magnetic observatories through a multiple station transfer function (the first CLFA linear filter) to generate a predicted local magnetic field time series at each of a set of locations where magnetotelluric impedance tensors had been previously obtained. The predicted magnetic fields are then projected through the impedance tensors (the second CLFA linear filter) to predict the horizontal vector components of the ground electric fields at those locations. In the final step, a nearest neighbor interpolation algorithm is used to project the predicted electric fields onto the path of powerlines that lie within the footprint of the

magnetotelluric sites. The CLFA method was found to run sufficiently fast to enable real-time prediction throughput to be achieved, barring solvable data acquisition difficulties, and was shown to produce predictions of high coherence and low misfit with the time series that were predicted. Improvements in the fidelity of the predicted electric fields may result from appending lower frequency impedance estimates from global-scale electrical conductivity models of the mid-to-lower mantle to the MT derived impedance tensors to more faithfully capture long period (e.g. diurnal) variations in the electric field. Despite existing limitations, the CLFA ground electric field yielded significantly lower misfits to electric field data actually measured at the MT sites than predictions made using either NERC [2013] guidelines or a proposed hybrid method. We attribute this to the CLFA method's incorporation of 3-D ground conductivity information through use of the full MT impedance tensors, rather than reliance of older regional 1-D models of ground conductivity that have been shown not to reflect the true complexity of the electric structure of the crust and mantle.

Acknowledgments and Data

The authors acknowledge the support of National Science Foundation GEOPRISMS and EarthScope Programs joint Award EAR-1053632 "Collaborative Research: Onshore-offshore MT investigation of Cascadia Margin 3D Structure, Segmentation and Fluid Distribution", and National Science Foundation EarthScope Program Cooperative Agreements EAR-0733069 and EAR-1261681 respectively through subcontracts 75-MT and 05-OSU-SAGE "Operation and Management of EarthScope Magnetotelluric Program" from Incorporated Research Institutions for Seismology (IRIS) to Oregon State University to acquire the MT data used in this work.

L Bonner acknowledges the support of a Graduate Teaching Assistantship from the College of Earth, Ocean and Atmospheric Sciences at Oregon State University that made this work possible.

The co-author acknowledges the assistance of his co-PIs under NSF award EAR-1053632 and collaborative project awards, Paul Bedrosian, Kerry Key, Dean Livelibrooks and Gary Egbert, as well as National Geoelectromagnetic Facility laboratory manager Brady Fry, and a host of students for their efforts to acquire the primary MT data set cited in this work. The authors also acknowledge the efforts of Dr. Antti Pulkkinen and team partners under support from the NASA Living with a Star Program for coordinating a series of workshops and collaborations that led to this paper being written.

All EarthScope MT Transportable Array data is available for public access from the IRIS Data Management System. MT time series may be downloaded from http://ds.iris.edu/gmap/_US-MT, and MT transfer functions may be downloaded from: http://ds.iris.edu/gmap/spud/emtf. MT data obtained under the support of NSF award EAR-1053632, cited in this work, will be available for download from the above URLs following the end of a two-year proprietary period at the conclusion of that project's period of performance.

References

Bahr, K., Interpretation of the magnetotelluric impedance tensor: regional induction and local telluric distortion, *J. Geophs.* **62**, 119 – 127 (1988).

Barber C., *et al.*, The Quickhull algorithm for convex hulls, *ACM Transactions on Mathematical Software* **22**, 469 – 483 (1996).

Bedrosian, P. A., and J. J. Love, Mapping geoelectric fields during magnetic storms: Synthetic analysis of empirical United States impedances, Geophys. Res. Lett., 42(23), 10,160– 10,170, doi:10.1002/2015GL066636, (2015).

Boteler D., Pirjola R., & Nevalinna H., The effects of geomagnetic disturbances on electrical systems at the Earth's surface, *Adv. Space Res.* **22**, 17-27 (1998).

Cagniard, L., Basic theory of the magneto-telluric method of geophysical prospecting, *Geophysics* **18**, 603 – 635 (1953).

Chave A. & Thomson D., Bounded influence magnetotelluric response function estimation, *Geophys. J. Int.* **157**, 988 – 1006 (2004).

Cherevatova, M., M. Yu. Smirnov, T. Korja, L.B. Pedersen, J. Ebbing, S. Gradmann, M. Becken, and MaSca Working Group, Electrical conductivity structure of north-west

Fennoscandia from three-dimensional inversion of magnetotelluric data, Tectonosphysics, 653, 20-32, doi: doi:10.1016/j.tecto.2015.01.008 (2015).

Chew, L., Constrained Delaunay triangulations, *Algorithmica* **4**, 97 – 108 (1989).

Cochran W., *et al.*, What is the Fast Fourier Transform, *IEEE Transactions on Audio and Electroacoustics* **15**, 45 – 55 (1967).

Eisel, M. & Egbert, G.D., On the stability of magnetotelluric transfer function estimates and the reliability of their variances, *Geophys. J. Intl.*, **144**, 65-82 (2001).

Egbert G. & Booker J., Robust estimation of geomagnetic transfer functions, *Geophys. J. R. ast. Soc.* **87**, 173 – 194 (1986).

EPRI, *One-Dimensional Earth Resistivity Models for Selected Areas of Continental United States and Alaska.* EPRI, ed R. Lordan, Palo Alto, CA. 1026430 (2002).

Evans R., *et al.*, Electrical structure of the central Cascadia subduction zone: The EMSLAB Lincoln Line revisited, *Earth and Planetary Science Letters* **402**, 265 – 274 (2014).

Gamble T., Goubau W., & Clarke J., Magnetotellurics with a remote magnetic reference, *Geophysics* **44**, 53 – 68 (1979).

Geomag Library, an Open Source Python Library provided by the US Geological Survey Geomagnetism Program, https://github.com/usgs/geomag-algorithms, accessed on September 1, 2016.

Groom, R.W. & R.C. Bailey, Decomposition of magnetotelluric impedance tensors in the presence of local three-dimensional galvanic distortion, *J. Geophys. Res.*, **94**, No. B2, `9`3-`915 (1989).

Imamura, N. & A. Schultz, Full waveform time domain solutions for source and induced magnetotelluric and controlled-source electromagnetic fields using quasi-equivalent time domain decomposition and GPU parallelization, Abstract GP24A-01 presented at 2015 Fall Meeting, AGU, San Francisco, Calif., 14-18 Dec. (2015).

Janssen A., *et al.*, Adaptive interpolation of discrete-time signals that can be modeled as autoregressive processes, *IEEE Transactions on Acoustics, Speech, and Signal Processing* **34**, 317 – 330 (1986).

Jones A., *et al.*, A comparison of Techniques for Magnetotelluric Response Function Estimation, *Journal of Geophysical Research* **94**, 14,201 – 14,213 (1989).

Jones, A.G., M.R. Muller, R.L. Evans, P. Cole, T. Ngwisanyi, D. Hutchins, C.J.S. Fourie, S.F. Evans, A. Mountford, W. Pettit, and the SAMTEX team, Southern African lithospheric geometries deduced from electromagnetic imaging: the SAMTEX project, *Geophys. Res. Abstracts* **10**, *EGU2008-A-08560, SRef-ID: 1607-7962/gra/EGU2008-A-08560*, (2008).

Jones, A.G., Three-dimensional galvanic distortion of three-dimensional regional conductivity structures: comment on three-dimensional joint inversion for magnetotelluric resistivity and static shift distributions in complex media by Yutaka Sasaki and Max A. Meju, *J. geophys. Res.*, **116,** B12104, doi:10.1029/2011JB008665 (2011).

Kataoka R. & Pulkkinen A., Geomagnetically induced currents during intense storms driven by coronal mass ejections and corotating interacting regions, *Journal of Geophysical Research* **113**, A03S12 (2008).

Kelbert, A., A. Schultz & G. Egbert, Global electromagnetic induction constraints on transition-zone water content variations, Nature 460, 1003-1006, doi:10.1038/nature08257 (2009).

Kelbert, A., G.D. Egbert and A. Schultz, IRIS DMC Data Services Products: EMTF, The Magnetotelluric Transfer Functions, doi:10.17611/DP/EMTF.1 (2011).

Kelbert, A., G. D. Egbert. & C. deGroot-Hedlin , Crust and upper mantle electrical conductivity beneath the Yellowstone Hotspot Track." *Geology* 40.5: 447-450 (2012).

Khosravi, L. & E. Johansson, *Evaluation of the GIC module in PSS/E*, Master of Science Thesis, Department of Energy and Environment, Chalmers University of Technology, Gothenburg, Sweden (2015).

Ku, H.H., Notes on the use of propagation of error formulas, *Journal of Research of the National Bureau of Standards – C. Engineering and Instrumentation*, **70C**, No. 4, 263-273 (1966).

Lotz S. & Cilliers P., A solar wind-based model of geomagnetic field fluctuations at a mid-latitude station, *Advances in Space Research* **55**, 220 – 230 (2015).

Love J. & Swidinsky A., Time causal operational estimation of electric field induced in the Earth's lithosphere during magnetic storms, *Geophys. Res. Lett.* **41**, 2266-2274 (2014).

Love, J.J., A. Pulkkinen, P.A. Bedrosian, S. Jones, A. Kelbert, E.J. Rigler, C.A. Finn, C.C. Balch, R. Rutledge, R.M. Waggel, A.T. Sabata, J.U. Kozyra & C.E. Black, Geoelectric hazard maps for the continental United States, *Geophys. Res. Lett.*, **43**, doi:10.1002/2016GL070469 (2016).

Meqbel N., *et al.*, Deep electrical resistivity structure of the northwestern U.S. derived from 3-D inversion of USArray magnetotelluric data, *Earth and Planetary Science Letters* **402**, 290–304 (2014).

Molinski T., Why utilities respect geomagnetically induced currents, *JASTP* **64**, 1765-1778 (2002).

NERC, Application guide computing geomagnetically-induced current in the bulk power system,

1 – 39 (2013).

Ngwira C., *et al.*, Extended study of extreme geoelectric field event scenarios for geomagnetically induced current applications, *Space Weather* **11**, 121 – 131 (2013).

Ngwira C., *et al.*, Characteristics of extreme geoelectric fields and their possible causes: Localized peak enhancements, *Geophysical Research Letters* **42**, (2015).

Overbye, T.J., T.R. Hutchins, K. Shetye, J. Weber & S. Dahman, Integration of geomagnetic disturbance modeling into the power flow: A methodology for large-scale system studies, North American Power Symposium (NAPS), 10.1109/NAPS.2012.6336365 (2012).

Pirjola R., Fundamentals about the flow of geomagnetically induced currents in a power system applicable to estimating space weather risks and designing remedies, *JASTP* **64**, 1967-1972 (2002).

Pirjola R., Boteler D., *et al.*, Prediction of geomagnetically induced currents in power transmission systems, *Adv. Space Res.* **26**, 5 – 14 (2000).

Pirjola R., Viljanen A., *et al.*, Space weather risk in power systems and pipelines, *Phys. Chem. Earth* **25**, 333 – 337 (2000).

Pulkkinen A., Amm O., Viljanen A., Ionospheric equivalent current distributions determined with the method of spherical elementary current systems, *Journal of Geophysical Research* **108**, SIA (2003).

Pulkkinen A., *et al.*, Geomagnetic storm of 29-31 October 2003: Geomagnetically induced currents and their relation to problems in the Swedish high-voltage power transmission system, *Space Weather* **3**, S08C03 (2005).

Pulkkinen A., Pirjola R., Viljanen A., Determination of ground conductivity and system parameters for optimal modeling of geomagnetically induced current flow in technological systems, *Earth Planets and Space* **59**, 999 – 1006 (2007).

Pulkkinen A., *et al.*, First-principles modeling of geomagnetically induced electromagnetic fields and currents from upstream solar wind to the surface of the Earth, *Ann. Geophys.* **25**, 881 – 893 (2007).

Pulkkinen A., *et al.*, Generation of 100-year geomagnetically induced current scenarios, *Space Weather* **10**, S04003 (2012).

Pulkkinen A., *et al.*, Regional-scale high-latitude extreme geoelectric fields pertaining to geomagnetically induced currents, *Earth Planets and Space* **67:93**, (2015).

Schultz, Adam, and Geoffrey Pritchard. "Three-Dimensional Inversion for Large-Scale Structure in a Spherical Domain'." Three Dimensional Electromagnetics, SEG Geophysical Developments Series 7, 451-476 (1999).

Schultz, A., EMSCOPE: A continental scale magnetotelluric observatory and data discovery resource, *Data Science* Journal 8, P IGY6-IGY20, http://doi.org/10.2481/dsj.GG_IGY-009 (2009).

Schultz, A., P. Bedrosian, K. Key, D. Livelybrooks, G.D. Egbert, E. Bowles-Martinez, P.E. Wannamaker, Magnetotelluric investigations of convergent margins and of incipient rifting: Preliminary results from the EarthScope MT Transportable Array and MT FlexArray deployments in Cascadia and in the North American Mid-Continent Region, *Amer. Geophy. U., Fall Meeting 2014, abstract #GP31A-3676* (2014).

Simpson, J.J., Current and Future Applications of 3-D Global Earth-Ionosphere Models Based on the Full-Vector Maxwell's Equations FDTD Method, *Surveys in Geophysics* **30**, Issue 2, pp 105–130, (2009).

Stearns S. & Hush D., *Digital Signal Analysis*, 460 p. (1990).

Sun, J., A. Kelbert, and G. D. Egbert. "Ionospheric current source modeling and global geomagnetic induction using ground geomagnetic observatory data." Journal of Geophysical Research: Solid Earth 120.10, 6771-6796 (2015).

Telford W., *et al.*, *Applied Geophysics* Ed. 2, 293 – 342 (1990).

Thiel, S., G. Heinson, A. Reid & K. Robertson, Insights into lithospheric architecture, fertilization and fluid pathways from AusLAMP MT, *ASEG Extended Abstracts 2016(1) 1-6*, doi: 10.1071/ASEG2016ab261 (2016).

Thomson, A.W.P., A.J. McKay, E. Clarke & S.J. Reay, Surface electric fields and geomagnetically induced currents in the Scottish Power grid during the 30 October 2003 geomagnetic storm, *Space Weather* **3**, S11002, doi:10.1029/2005SW000156 (2005).

Utada, H. and H. Munekane, On galvanic distortion of regional three-dimensional magnetotelluric impedances, *Geophys. J. Int.* 140, 385-398, (2000).

Vanhamaki H., *et al.*, Deriving the geomagnetically induced electric field at the Earth's surface

From the time derivative of the vertical magnetic field, *Earth Planets Space* **65**, 997 - 1006 (2013).

Van Rossum, G., *The Python Language Reference Manual*, Fred L. Drake, Jr. (Editor), published by Network Theory Ltd., ISBN 978-906966-14-0 (2011).

Viljanen A., *et al.*, Modeling geomagnetically induced currents during different ionospheric situations, *Journal of Geophysical Research* **104**, 28,059 – 28,017 (1999).

Viljanen A., *et al.*, Fast computation of the geoelectric field using the method of elementary current systems and planar Earth models, *Annales Geophysicae* **22**, 101 – 113 (2004).

de Villiers J. & Cilliers P., Applying inversion techniques to derive source currents and geoelectric fields for geomagnetically induced current calculations, *Ann. Geophys.* **32**, 1263 – 1275 (2014).

Wait J., Theory of magneto-telluric fields, *Journal of Research of the National Bureau of Standards* **66D**, 509 – 541 (1962).

Wei L., *et al.*, Surface electric fields for North America during historical geomagnetic storms, *Space Weather* **11**, 451 – 462 (2013).

Weigel R., Vassiliadis D., Klimas A., Coupling of the solar wind to temporal fluctuations in ground magnetic fields, *Geophysical Research Letters* **29**, 1915 (2002).

Yun, L., X. Xiaochun, L. Bin and P. Jinfeng, Time-frequency analysis based on the S-transform, *Intl. J. of Signal Processing, Image Processing and Pattern Recognition* **6**, No. 5, http://dx.doi.org/10.14257/ijsip.2013.6.5.22 (2013).

Zhang T. & Schultz A., EXORCISE – An algorithm for detection of spurious values and prediction of missing data, *Computers and Geoscience* **16**, 1027-1065 (1990).

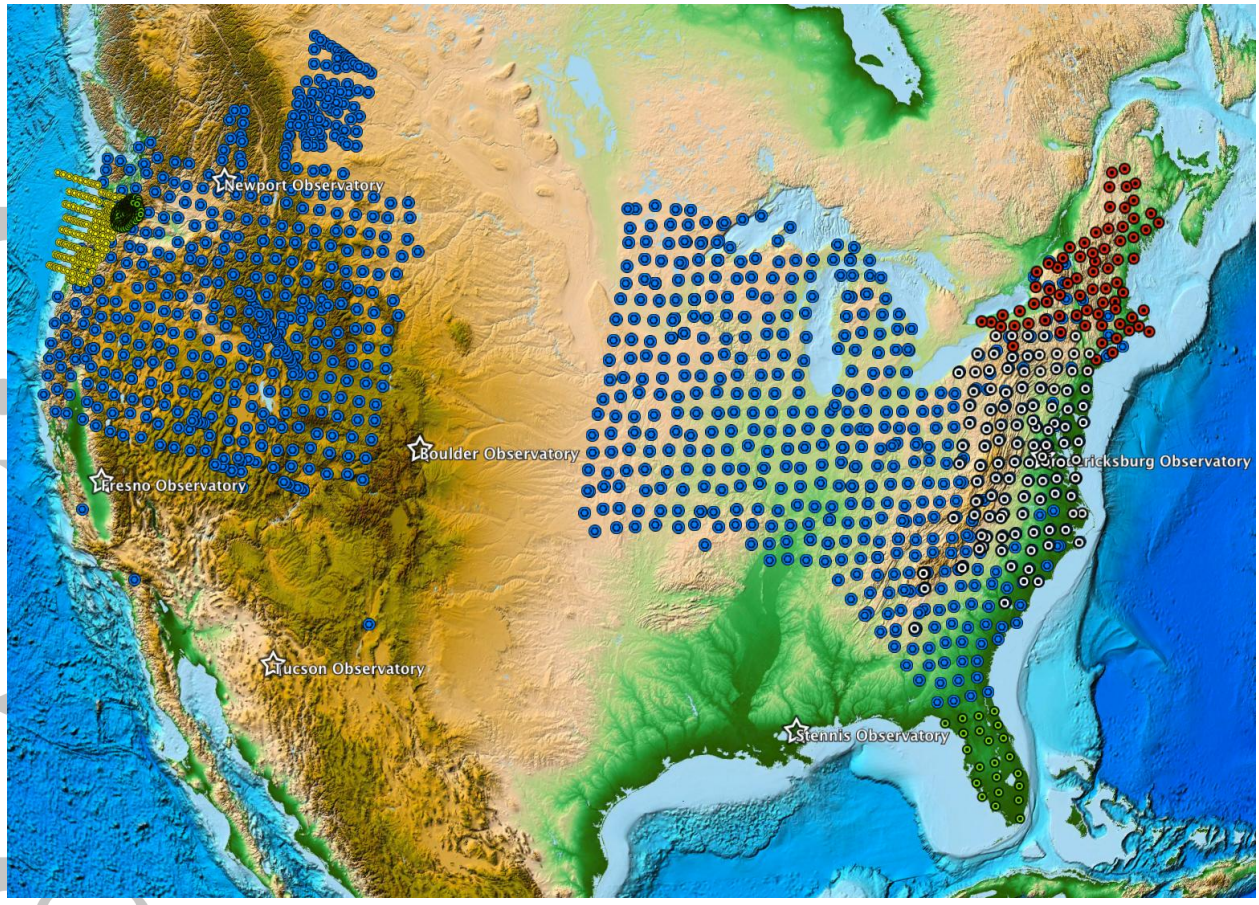

Figure 1: Locations of NSF EarthScope Program Magnetotelluric Transportable Array (MT TA) stations. Stations completed between 2006 – 2015 are shown as blue symbols (the Canadian stations were provided by the University of Alberta [M. Unsworth, pers. comm., 2011], and the higher density cross-shaped array centered on western Wyoming by the University of California, San Diego [C. deGroot-Hedlin, pers. comm., 2009]; all other sites were EarthScope MT TA sites acquired on a nominal 70 km station spacing grid under the direction of Oregon State University). The Peninsular Florida stations (green symbols) were acquired by the US Geological Survey [P. Bedrosian, pers. comm., 2016], EarthScope MT TA stations completed under the direction of Oregon State University in 2016 (white dots), and currently being installed and planned for completion by Oregon State University in 2016-2017 (red dots) are also shown. The locations of the US Geological Survey permanent magnetic observatory network stations in the continental US are marked with white stars (the

magnetic observatory at Honolulu, Hawaii, which is not shown, was also used in the analyses reported here). The small yellow symbols are the locations of the EarthScope-GeoPRISMS program MT station locations in and offshore southwest Washington and western Oregon used in the present study. Adjoining that array, the small green symbols are the locations of a high-resolution wideband MT study not used in the present study.

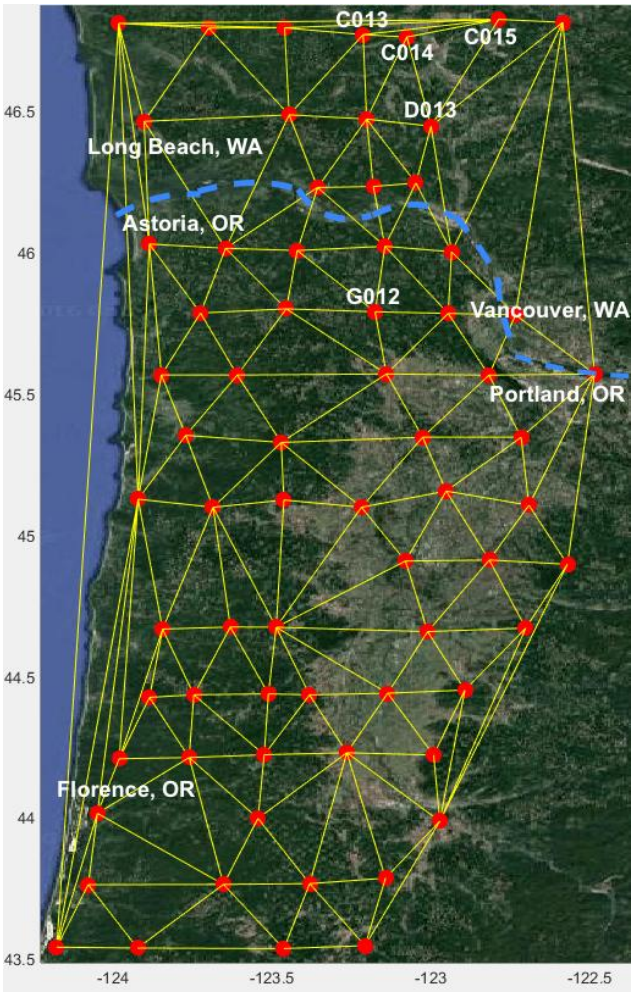

Figure 2: Map of the Delaunay triangulation formed by using the western Oregon and southwestern Washington portion of the EarthScope-GeoPRISMS project EAR-1053632 MT array sites used in the present work (these comprise most of the land MT stations that appear as small yellow symbols in Figure 1). The area displayed extends north-south ~370 km and east-west ~130 km, northward to just south of the Olympic Peninsula and just west of Seattle in the state of Washington, south to approximately the latitude of Coos Bay at the southern Oregon coast, and from the Pacific coast to the west and the foothills of the Cascade volcanic range to the east. The dashed blue line marks the border between Washington and Oregon, along the path of the Columbia River. In contrast to the EarthScope MT Transportable Array stations shown in Figure 1 with their nominal 70-km station spacing (blue, white and red symbols), for this project the station density was approximately three times finer. The MT

station locations are at the vertices of the Delaunay triangles, marked by a red dot. The axes are marked in degrees of latitude (y-axis) and longitude (x-axis), respectively. The identification of the nearest neighboring MT stations to any location within the MT array, such as the path of power lines, is based on construction of Delaunay triangles, as shown here and discussed in Sections 3 and 4 of this paper.

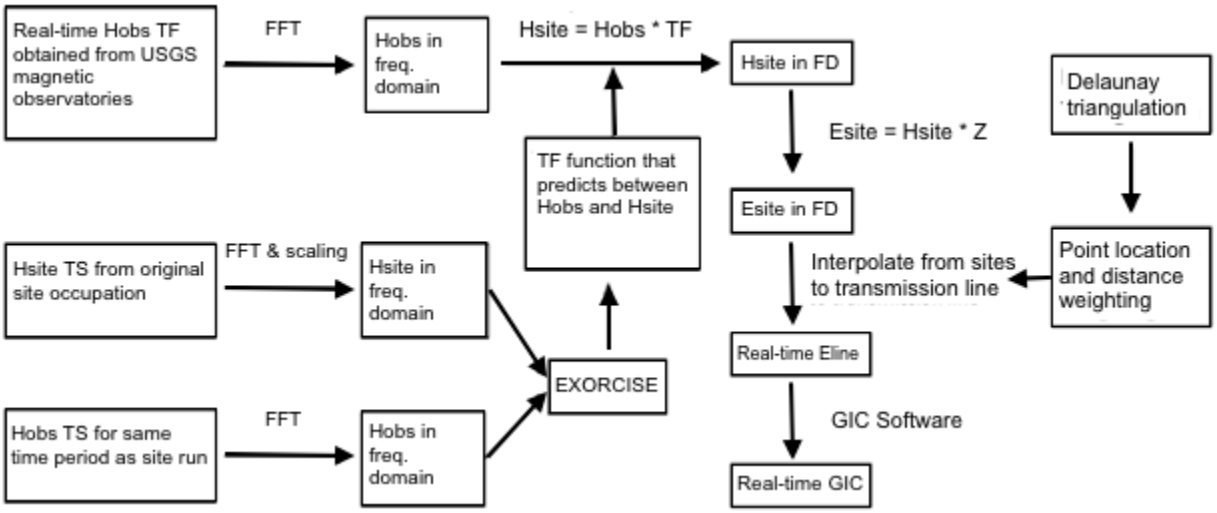

Figure 3: Data flow chart of computations necessary to transform real-time magnetic time series into predicted total electric field values for GIC predictions, where **FFT** indicates Fast Fourier Transformation, **TS** are the time series, and **FD** indicates frequency domain.

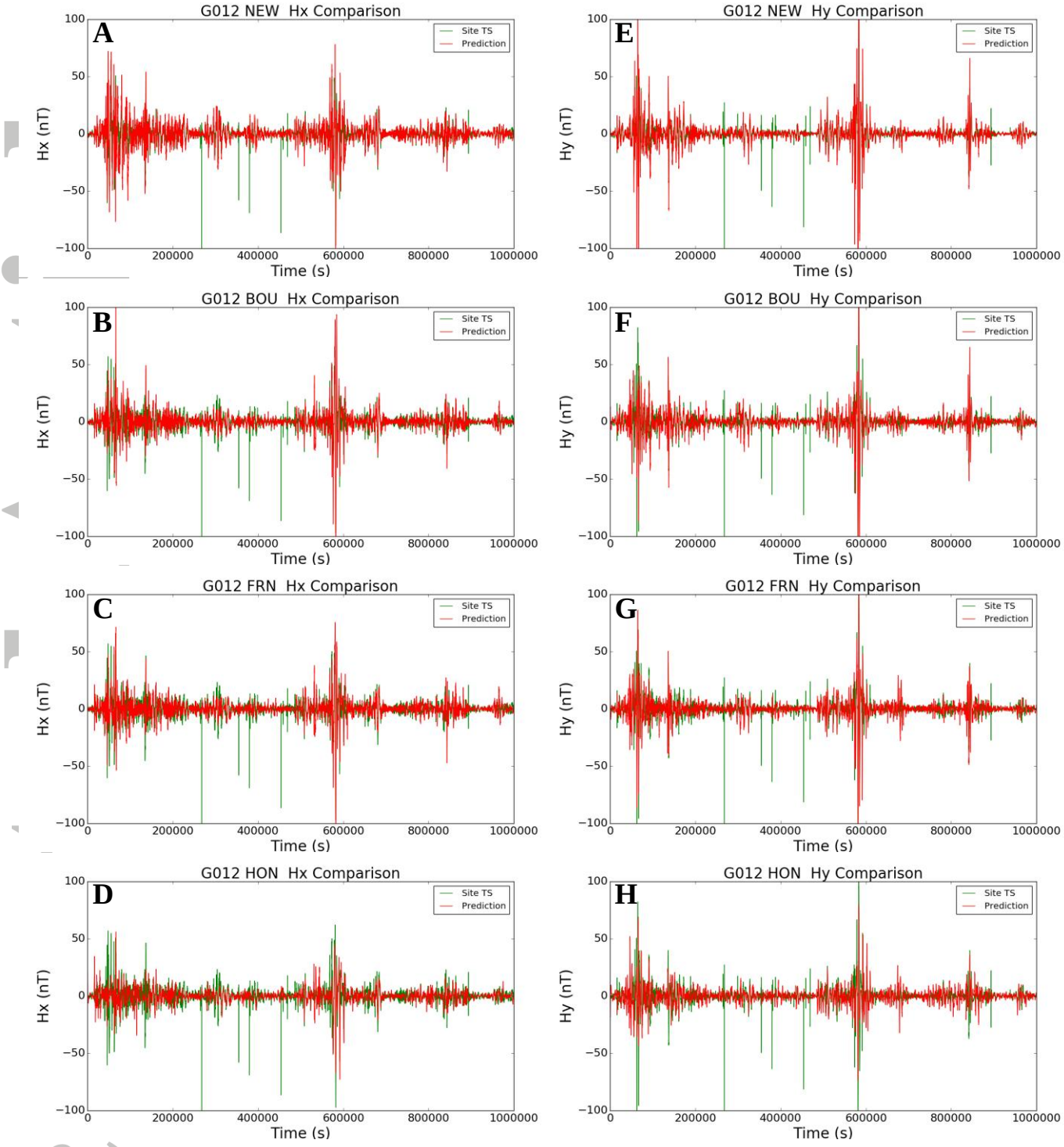

Figure 4: Comparisons between the actual recorded (green curves) and predicted (red curves) horizontal components of magnetic field variations time series at MT station G012 near Portland, Oregon based on projections of magnetic fields from individual magnetic

observatories through single-station transfer functions. Data from the USGS magnetic observatories at Newport Washington, Boulder Colorado, Fresno California, and Honolulu Hawaii were used in this and other examples throughout this paper. A time series window length of 10^6 s (~11.6 d) is shown. (A) – (D) show the recorded north-south (x) component of the magnetic fields at station G012 and those predicted at that site by projection of data from the remote magnetic observatories at Newport (A), Boulder (B), Fresno (C), and Honolulu (D). (E) – (F) show the corresponding east-west (y) components of the measured and predicted magnetic fields.

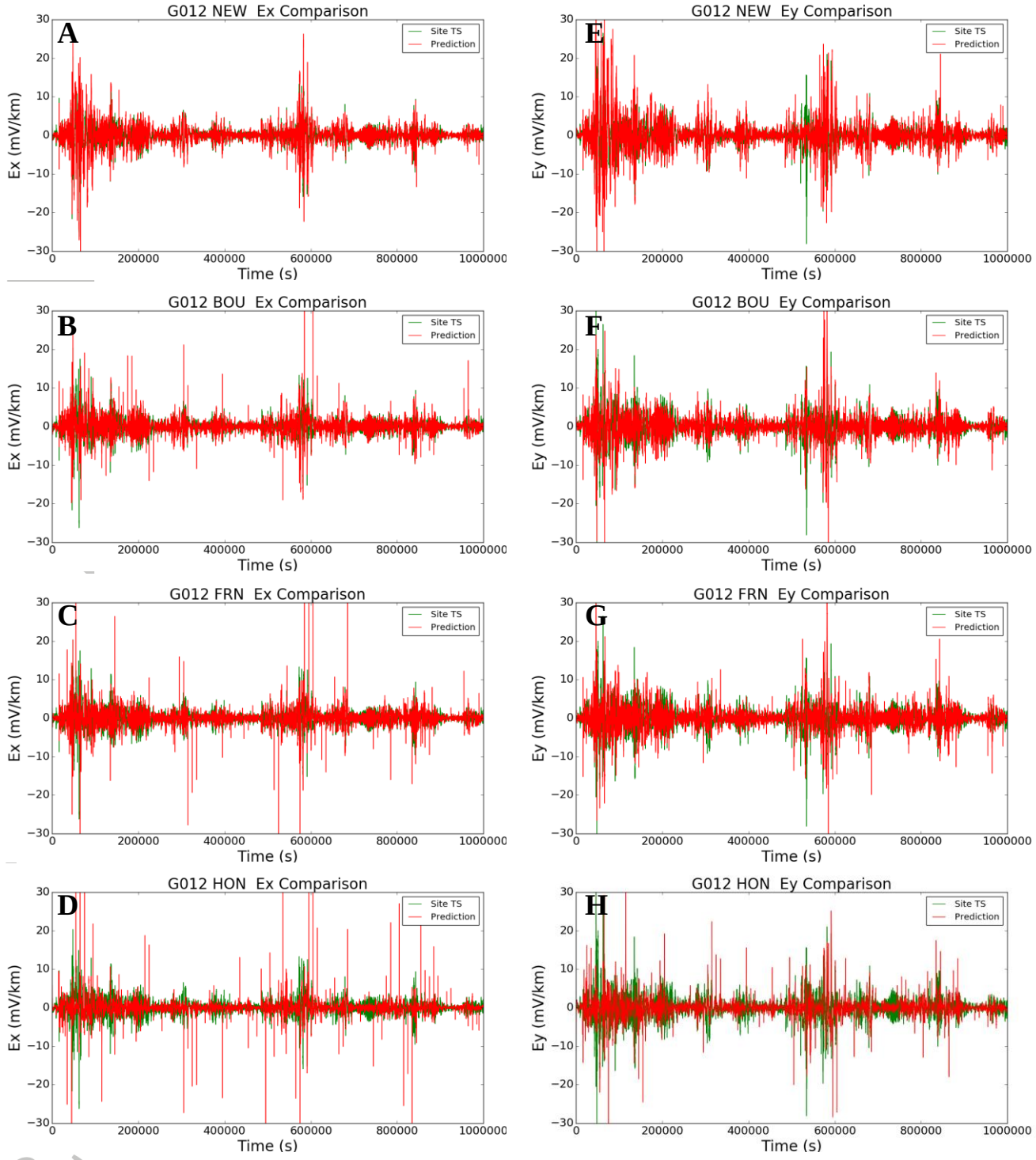

Figure 5: Comparisons between the actual recorded (green curves) and predicted (red curves) horizontal components of electric field variations time series at MT station G012 near Portland, Oregon based on projections of magnetic fields from individual magnetic observatories through single-station transfer functions following which predicted magnetic

fields are projected through the impedance tensor for station G012 to yield predicted electric fields. Data from the USGS magnetic observatories at Newport Washington, Boulder Colorado, Fresno California, and Honolulu Hawaii were used in this example. A time series window length of 1 million seconds is shown. (A) – (D) show the recorded north-south (x) component of the electric fields at station G012 and those predicted at that site by projection of data from the remote magnetic observatories at Newport (A), Boulder (B), Fresno (C), and Honolulu (D) and application of the impedance tensor at G012. (E) – (F) show the corresponding east-west (y) components of the measured and predicted electric fields.

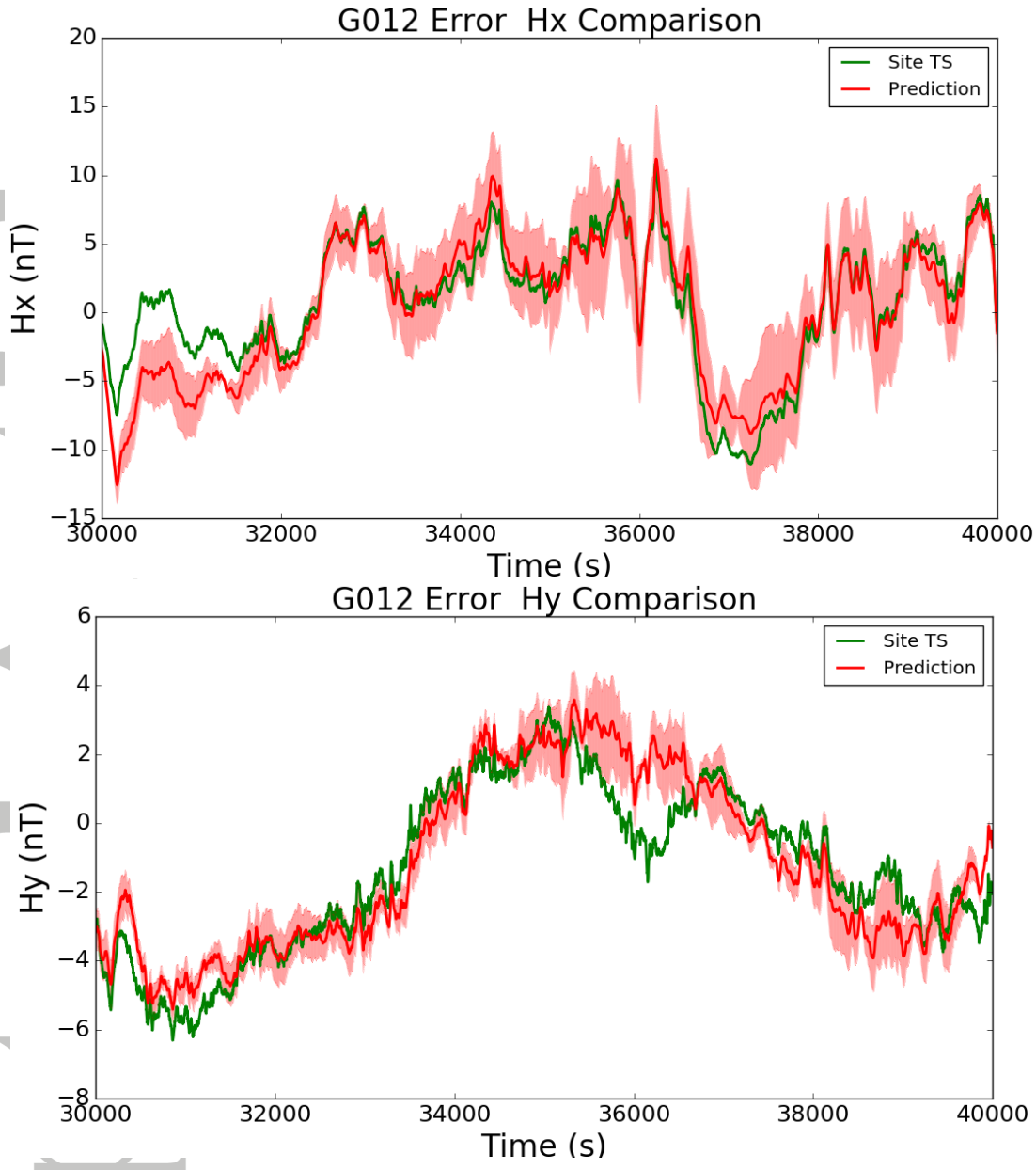

Figure 6: High-pass filtered magnetic field time series for data recorded at MT site G012 (green curves) and for data predicted for that location ±95% confidence interval (red curves) by projection of vector magnetic field variation data recorded at the four magnetic observatories, projected through a multiple station transfer function, shown in the (A) north-south (*x*) and (B) east-west (*y*).

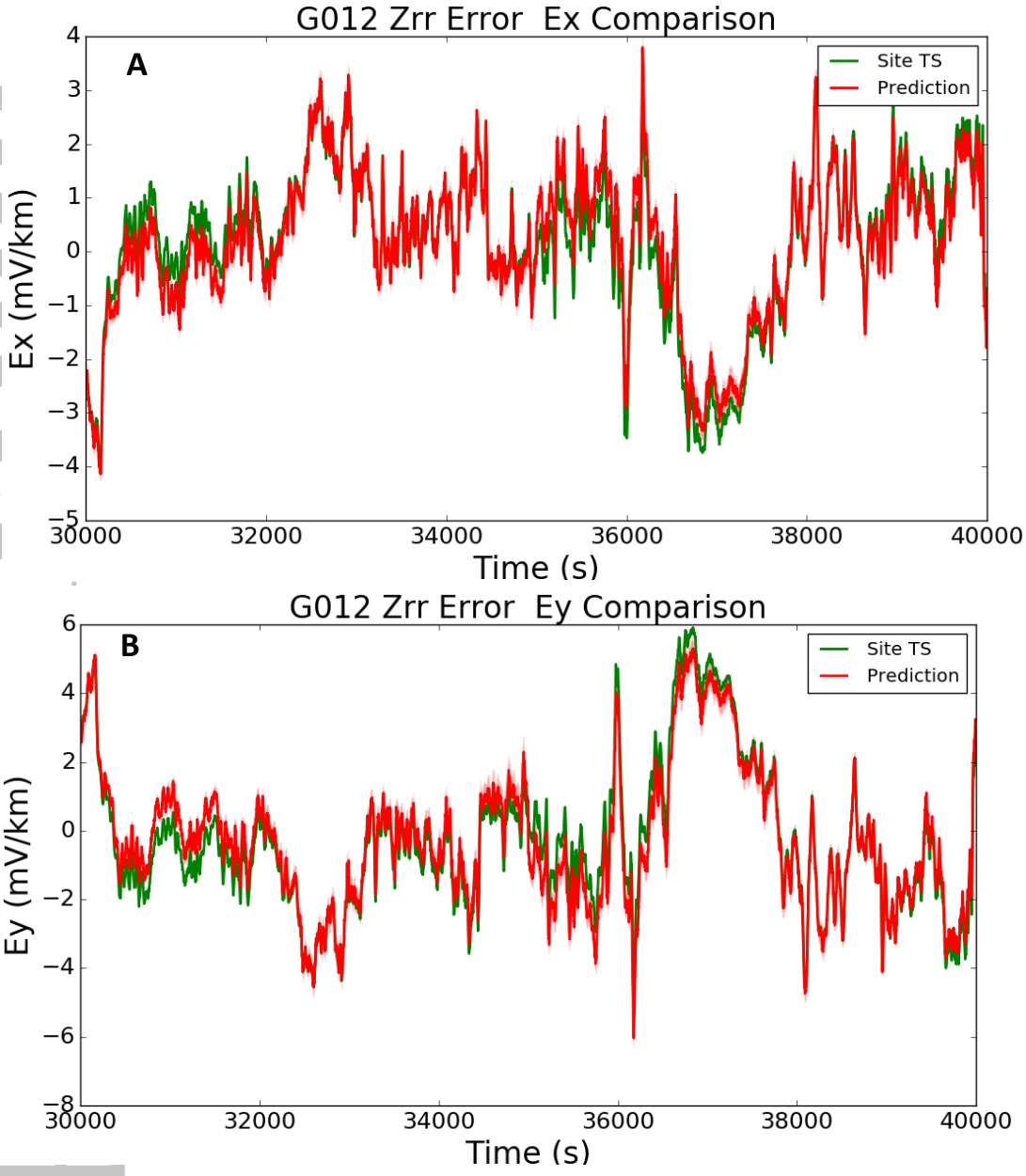

Figure 7: High-pass filtered electric field time series for data recorded at MT site G012 (green curves) and for data predicted for that location ±95% confidence interval (red curves) by projecting the locally recorded magnetic field data at that site through the local impedance tensor to yield the prediction of the local electric field at that site. Two sets of orthogonal electric field components are shown in the (A) north-south (*x*) and (B) east-west (*y*) directions.

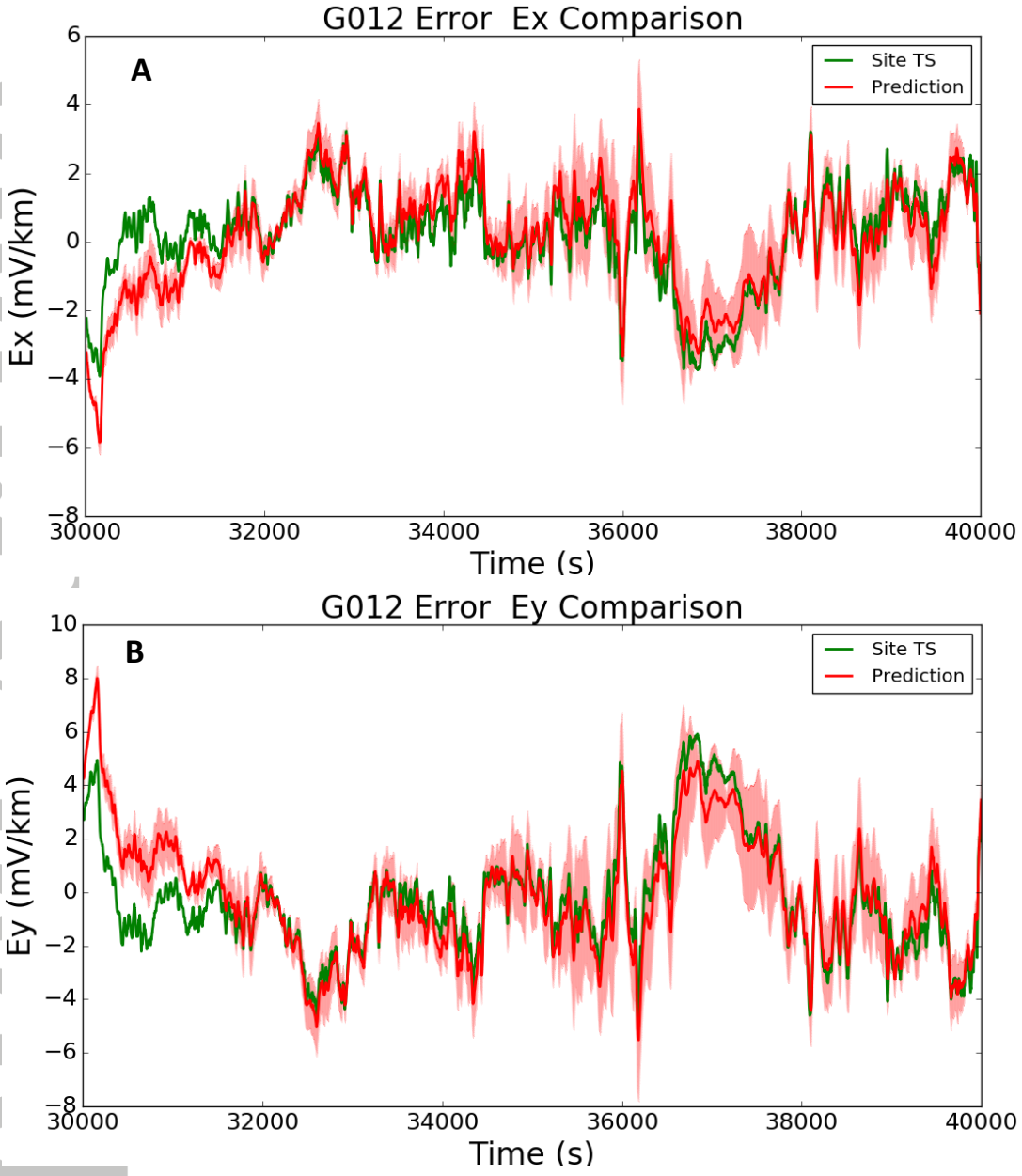

Figure 8: High-pass filtered electric field time series for data recorded at MT site G012 (green curves) and for data predicted for that location ±95% confidence interval (red curves) by projecting the vector magnetic field variation data recorded at the four magnetic observatories through a multiple station transfer function, resulting in a predicted magnetic field that is then projected through the local impedance tensor to yield the prediction of the local electric field at that site. Two sets of orthogonal electric field components are shown in the (A) north-south (x) and (B) east-west (y) directions.

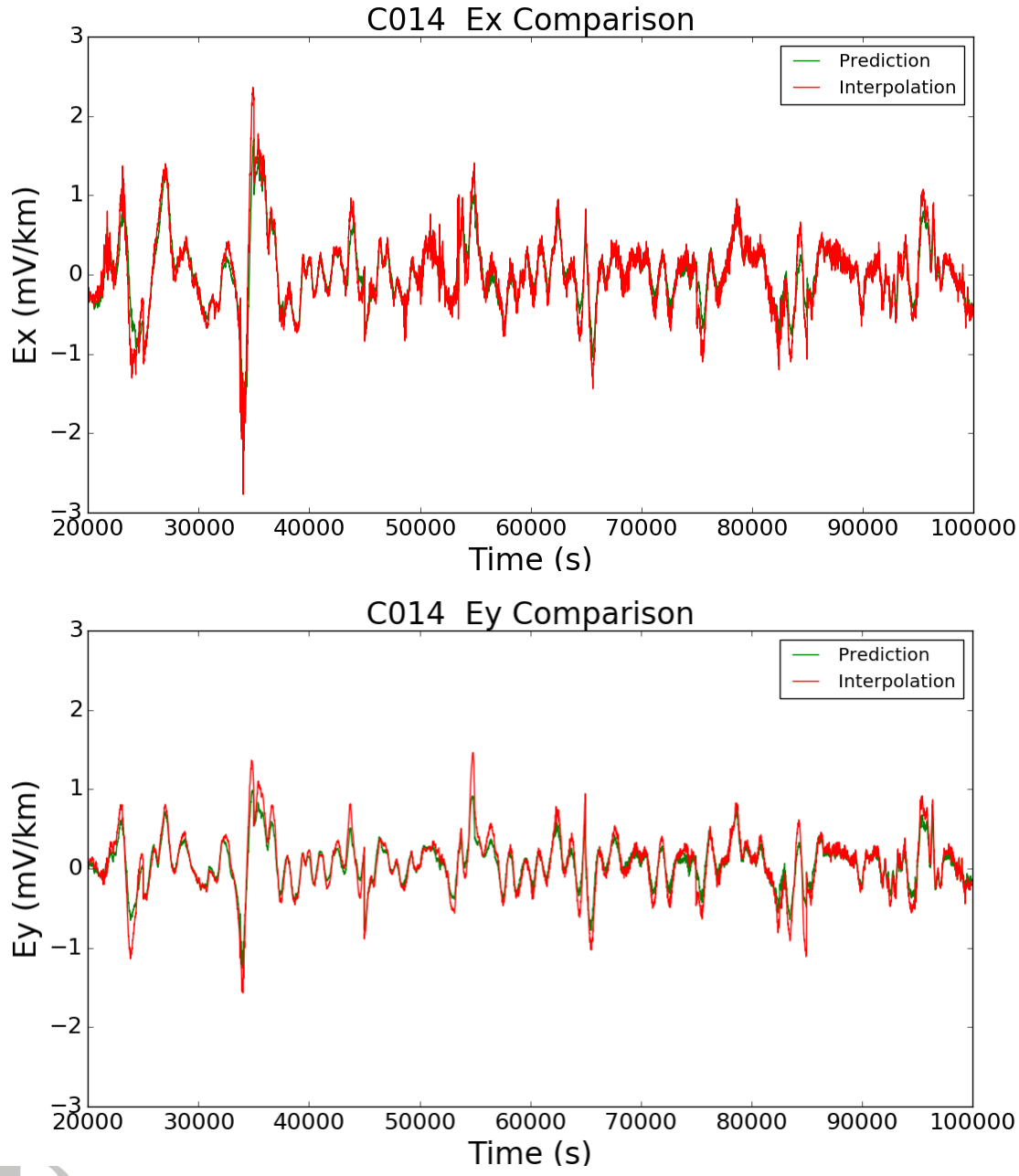

Figure 9: CLFA prediction of the north-south (E_x) (top plot) and east-west (E_y) (bottom plot) electric field components at MT station C014 (red curves) and nearest neighbor interpolation by distance-weighted averaging of the CLFA predictions of these same components from MT stations C013, C015 and D013 (see Figure 2 for station locations).

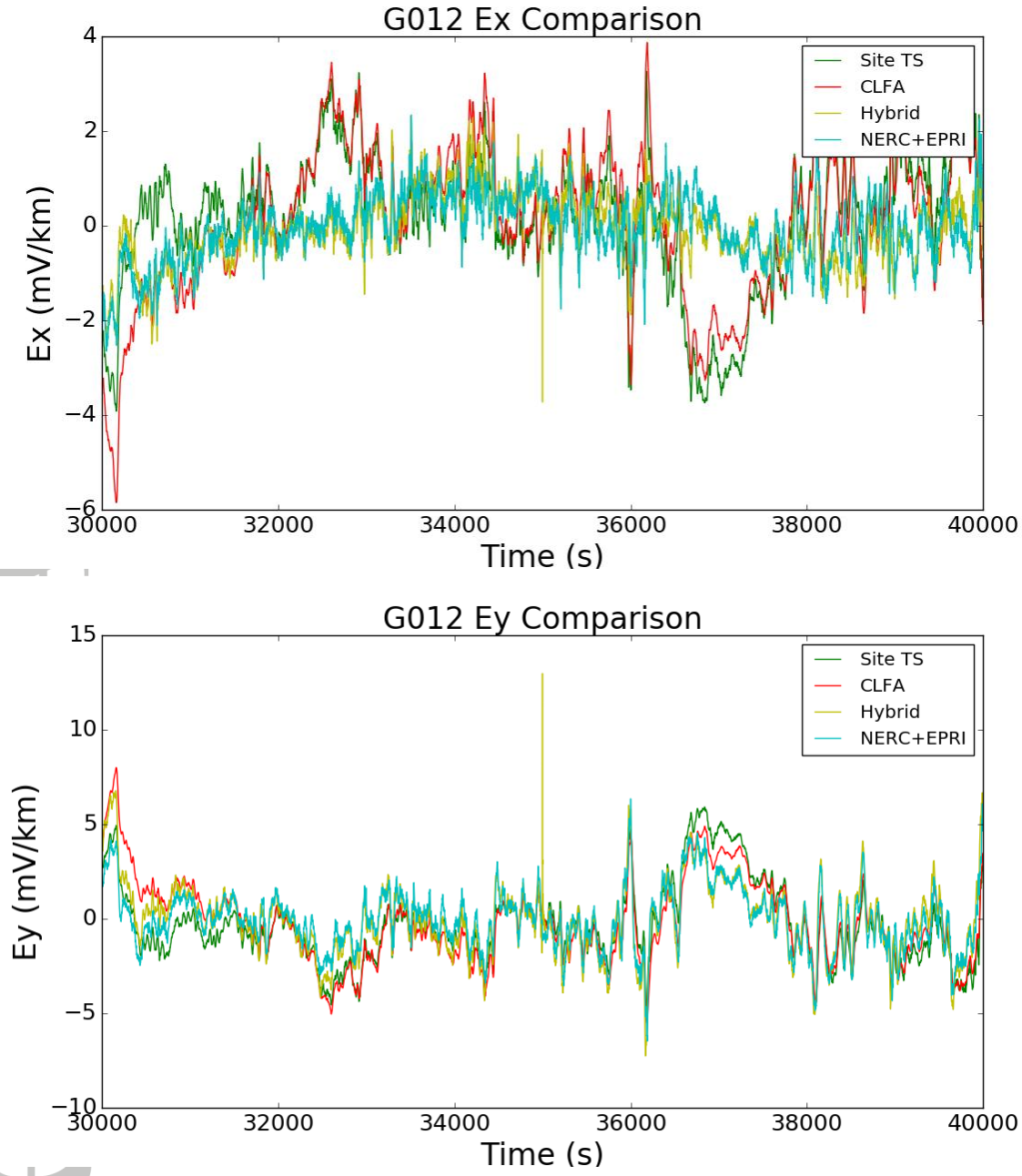

Figure 10: High-pass filtered electric field time series for data recorded at MT site G012 (green curves) and for electric field data predicted for that location using NERC (cyan curves), hybrid (yellow curves), and our cascading linear filter algorithm (red curves), in the north-south (*x*) (top panel) and east-west (*y*) (bottom panel) directions for a 10,000 s time series section.

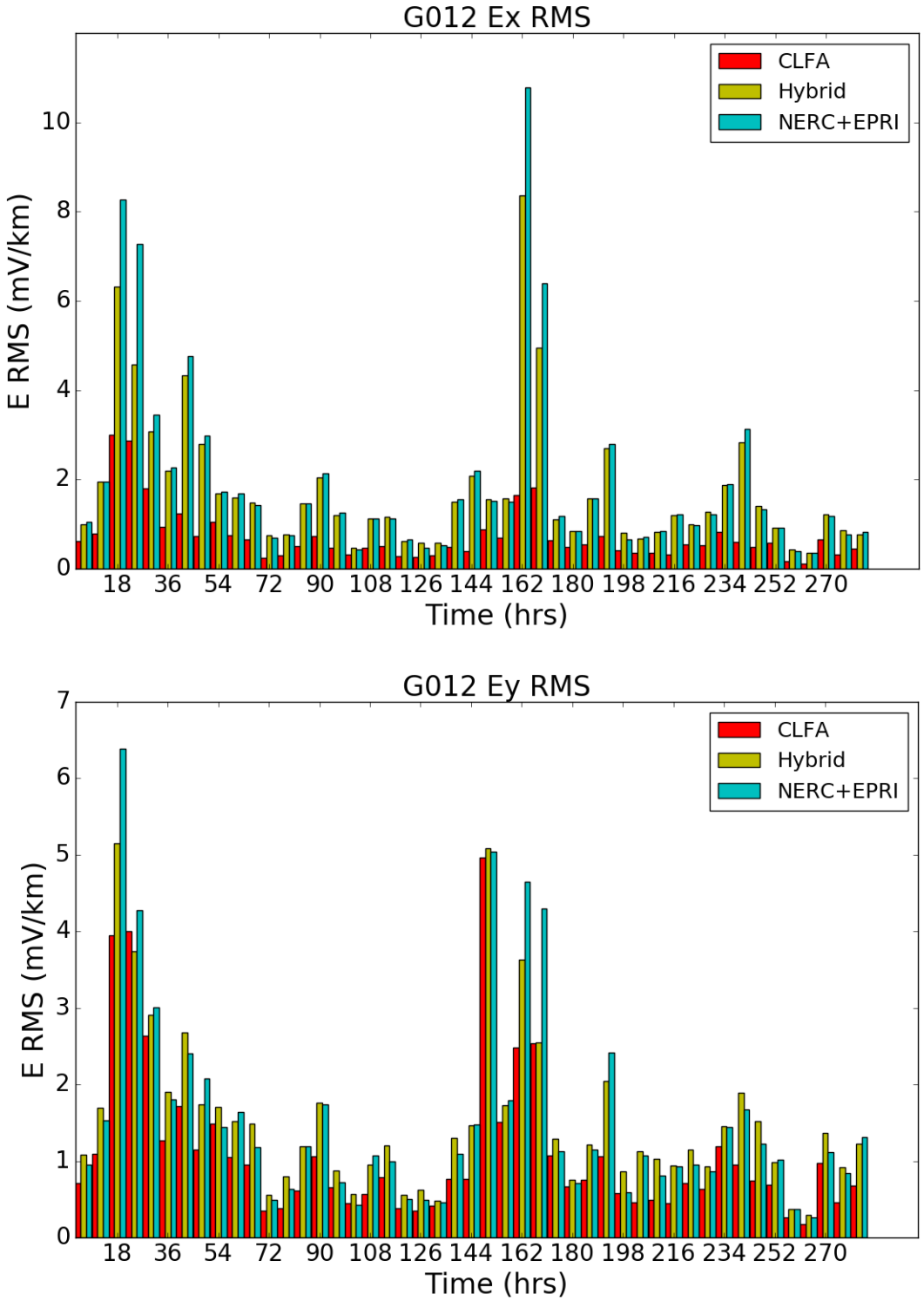

Figure 11: RMS misfit between the north-south (E_x) (top plot) and east-west (E_y) (bottom plot) electric field components actually measured at MT station location G012 and those predicted by the NERC (cyan), Hybrid (yellow) and the CLFA (red) methods, calculated within 6-hour bins for a 10^6 s time series section.